

Alma Mater Studiorum – Università di Bologna

Dipartimento di Fisica e Astronomia “Augusto Righi”
Laurea Magistrale in Fisica del Sistema Terra

Seagrass meadows as a nature based solution

Presentata da:

Leonardo Romano

Relatore:

Prof. Paolo Oddo

Correlatore:

Dott. Jacopo Alessandri

Anno Accademico 2023 - 2024

Appello V

Contents

1	Introduction	3
1.1	Geographical and Environmental Setting	4
1.2	Ecological Significance	4
1.3	Environmental Challenges	5
1.4	Nature based solutions	5
1.5	Importance of Hydrodynamic Analysis	6
1.6	Overview of subsequent chapters	6
2	SHYFEM-MPI model	8
2.1	Governing equations	8
2.2	Boundary conditions	10
3	Model setup	13
3.1	Domain of simulation	13
3.1.1	Parameter Selection and Variability	14
3.2	Simulation setup	17
3.3	Datasets	18
3.4	Method of analysis	18
4	Analysis	20
4.1	Control Characterization	20
4.1.1	Vertical Profiles (Hovmöller Diagrams)	21
4.1.2	Vertical Profiles of Speed	22
4.1.3	Horizontal Maps at Surface and Bottom Layers	22
4.2	Seagrass Scenario Characterization	31
5	Ensemble of seagrass models	45
5.1	Basin-Averaged Temperature and Salinity	45
5.2	Hovmöller Diagrams of Differences	45
5.3	Horizontal maps of Ensemble STD at Surface and Bottom Layers	47
5.3.1	Velocity STD	47

5.3.2	Salinity STD	49
5.3.3	Sea Surface Height STD	49
5.4	Spectral Analysis of Ensemble STD	52
6	Conclusions	54
7	Bibliography	56

Chapter 1

Introduction

The Adriatic Sea is a semi-enclosed sea connected with the Mediterranean Sea only to the south end, bordered by Italy to the west and Slovenia, Croatia, Bosnia and Herzegovina, Montenegro and Albania to the east. It is a unique marine environment that sustains ecological and socio-economic processes in the surrounding regions. It is characterized by its varied geography and distinct climatic conditions, which together shape its complex marine environment. The stark differences in average depth between the northern and southern regions, coupled with the intricate and irregular bathymetry along the eastern coast, the vast freshwater afflux from the Alps in the shallow northern part, and a significant wind fetch SE/NW, all play a significant role in the dynamic nature of its water circulation. The Adriatic Sea remains an invaluable resource for the surrounding coastal regions, generating a significant contribution to fisheries, fish farming, and recreational activities, and a strategic route to maritime traffic. Beyond its historical heritage, the sea is facing mounting pressures from human activities and environmental changes, making it a focal point for studies on marine ecosystems and their sustainability. These physical and environmental features create unique challenges for understanding and modeling the Adriatic Sea hydro dynamics. Comprehension of the processes which regulate water circulation and nutrients transport, requires the implementation of sophisticated numerical methods capable of describing the iterations between physical, biological and chemical components. This work aims to study the effect of seagrass plant *Zostera Marin* in the Adriatic Sea, and through the comparison of 27 different parametrizations of seagrass, to understand the impact it would have on coastal circulation. Three parameters for seagrass modeling are used: leaf number density, leaf length and leaf width. For each of these parameters, three values were selected from previous literature, in order to represent the maximum and the minimum values observed, as well as their mean averages.

1.1 Geographical and Environmental Setting

Given the inherent complexity of studying the water circulation and the effects of seagrass on it, we approached it using numerical methods. This strategy allows us to simulate the dynamics in detail, yielding reliable and accurate results. The domain of the simulation extends along the western Adriatic coast, from the Po Delta System to south of Rimini. The western Adriatic coast is strongly influenced by the freshwater outflow from the Po River and the other smaller rivers, guided southward by the cyclonic circulation in the basin. This outflow significantly impacts salinity gradients, nutrient transport, and sediment deposition, all of which interact with seagrass meadows in the shallow coastal regions (Hemminga & Duarte, 2000). Seasonal wind patterns also play a critical role in shaping hydrodynamics behaviors. Bora and Sirocco winds, blowing from the northeast and southeast respectively, affect surface circulation and water mixing. Under normal meteorological conditions, the thermohaline circulation is dominant, with wind driven circulation as a secondary force. The Bora's horizontal shear induces cyclonic circulation in the northern Adriatic and anticyclonic circulation in the south, influencing the dispersion of nutrients and suspended sediments (Vianello et al., 2013). The long Sirocco fetch from SE coupled with tidal amplification due to the shallow average depth can generate extraordinary high tides across the region (Orlić et al., 1994).

1.2 Ecological Significance

Seagrasses are an essential component of the benthic layer of the Adriatic coast, contributing to sediment stabilization, providing habitat for aquatic organisms, facilitating nutrient cycling, and improving water quality (Orth et al., 2006; Hemminga & Duarte, 2000). The presence of marine plants increases turbulent mixing proportionally to the reduction in current velocity (Hemminga & Duarte, 2000). At the same time, seagrass meadows help prevent sediment resuspension, thereby decreasing water turbidity and allowing for enhanced photosynthesis (Orth et al., 2006). Another consequence of enhanced mixing is an increase in the oxygen concentration, which is more efficiently transported down from the surface, due to the higher shear velocity on top of the seagrass canopy (Duarte et al., 2010). In the northern Adriatic, *Zostera marina* typically forms patches in shallow coastal areas with depths of less than 10 m, where freshwater inputs are moderated and salinity remains relatively constant (Orth et al., 2006; Hemminga & Duarte, 2000). Its growth is limited in turbid waters influenced by riverine input, making its presence an indicator of relatively stable environmental conditions (Orth et al., 2006). Along the southern stretches of the western Adriatic, *Posidonia Oceanica* dominates, forming dense patches between depths of 20 m and 30 m. These meadows are crucial for maintaining biodiversity and are recognized as indicator species for seawater quality. However, recent analyses indicate a declining trend in their distribution due to

anthropogenic activities, such as anchoring and trawling (Short et al., 2007), as well as increasing sea water temperature.

1.3 Environmental Challenges

The Adriatic coast faces significant environmental challenges, many of which are linked to both natural processes and anthropogenic pressures. The northern Adriatic in particular, experiences unique challenges such as eutrophication, sedimentation, and the impacts of increasing urbanization and tourism, emphasizing the need for robust scientific approaches to understand and mitigate these effects. Freshwater inflows from the Alpine Rivers, which vary seasonally, influence salinity and nutrient levels along the coast. During summer, reduced precipitation leads to increased stratification and reduced water mixing, affecting sediment transport and nutrient distribution. Anthropogenic nutrient runoff from agricultural and urban areas promotes algal blooms. As these blooms decompose, they deplete oxygen levels, creating hypoxic conditions that harm aquatic life. Rising temperatures and altered precipitation patterns due to climate change exacerbate these conditions, increasing the frequency of extreme events like dystrophic crises (Rabalais et al., 2009). Invasive species, such as the blue crab (*Callinectes sapidus*), also pose a growing threat. These non-native species, introduced through human activities, disrupt local ecosystems by outcompeting native species and preying on economically important species like clams and mussels (Simberloff et al., 2013).

1.4 Nature based solutions

As defined at the 5th United Nations Environment Assembly (UNEA 5.2), nature based solutions (NbS) are “actions aimed at protecting, conserving, restoring, and sustainably managing natural or modified terrestrial, freshwater, coastal, and marine ecosystems, which address social, economic and environmental challenges effectively and adaptively, while simultaneously providing human well-being, ecosystem services, resilience and biodiversity benefits” (IUCN, 2020). These sustainable approaches enhance the resilience of the environment by leveraging the effectiveness of natural processes. By integrating ecological restoration programs in management strategies, NbS can deliver multiple benefits to the ecosystem, while operating in synergy with nature’s functions. The adoption of seagrass meadows is an important example of NbS which works by sequestering carbon from water, fostering diverse animal communities, acting as natural buffer, reducing wave energy and removing excess nutrients from waters (Duarte et al., 2010). Restoration of seagrass meadows in damaged environments can enhance the conditions for the survivability of other species and serves as a key indicator of ecological health and ecosystem recovery, reflecting the capacity of these systems to regain balance and support biodi-

versity and enhance ecosystem resiliency. Seagrass meadows are highly efficient carbon sinks, storing between 11% to 18% of the world's oceanic carbon despite covering only 0.1% of the ocean floor (Duarte et al., 2013). The rates of carbon capture for the 10% seagrass meadows with the largest carbon sink capacity have found to be well above the rates of carbon sink in undisturbed Amazonian forests, which are assumed to be the largest terrestrial carbon sinks (McLeod et al., 2011).

1.5 Importance of Hydrodynamic Analysis

Incorporating biological components, such as seagrass meadows, into hydrodynamic models represents a novel approach that bridges physical oceanography, marine biology, and ecological restoration. The water circulation, driven by tides, freshwater inputs and winds, is critical in maintaining the sea's functionality and ecological balancing effects. Developing accurate hydrodynamic model is essential for understanding the complex interactions between the forces at play and the responses of the area (Tagliapietra et al., 2009).

In this study, we analyzed the potential impact that seagrass could have on a fixed area of the Adriatic coastal zone by considering a constant distribution of seagrass. Furthermore, we evaluated whether variations in key seagrass characteristics, namely density, leaf length, and leaf width, could yield different hydrodynamic responses. These variations are critical, as a denser or longer-leaved seagrass bed can increase the resistance to flow, leading to reduced current speeds, altered turbulence levels, and modified sediment transport processes. Such changes can ultimately affect water clarity, nutrient cycling, and the overall ecological functioning of the coastal environment (Hemminga & Duarte, 2000; Orth et al., 2006).

Moreover, our investigation aims to provide deeper insights into the feedback mechanisms between seagrass morphology and hydrodynamics. Understanding these interactions is crucial not only for accurate modeling of natural coastal systems but also for the design of effective ecological restoration strategies aimed at preserving or enhancing these critical habitats. By comparing 27 different parameterizations of seagrass, our approach enables a thorough assessment of model sensitivity to seagrass characteristics, thereby advancing our understanding of their role in shaping local water circulation and ecological processes (Tagliapietra et al., 2009).

1.6 Overview of subsequent chapters

In the next chapter, we describe the hydrodynamic simulation model used to generate the simulation data. The method for implementing seagrass is further discussed in Chapter 3. In Chapter 4, the analysis first focuses on characterizing the control model, then

examines the differences between the seagrass model and the control model. In chapter 5 the seagrass models ensemble variability is studied through its standard deviation among different members. The results of this work are presented in chapter 6.

Chapter 2

SHYFEM-MPI model

This chapter is a review of J. Alessandri PhD thesis's chapter 1.2. The model adopted is a parallelized version of SHYFEM (System of Hydrodynamic Finite Element Modules) (Umgiesser et al., 2004), with the addition of seagrass and plant leaf flexibility. It solves the shallow water equations on an unstructured grid of triangular elements. This version of SHYFEM-MPI uses a finite element approach for the spatial integration and a semi-implicit method for the time integration. It is based on the solution of the primitive equations of motion under the assumption of incompressible fluid, after applying the Boussinesq and hydrostatic approximations. The model runs on an unstructured B-type Arakawa grid, where the vector components of the model are computed at the cell corners, while the scalar components are solved at the cell centers. The main advantage of adopting an unstructured grid is the flexibility to represent irregular coastlines, and reducing errors associated with grid misalignment. The finer resolution near the coastline allows for a more accurate representation of shallow water processes, which are crucial for understanding interactions between seagrass meadows and hydrodynamics. By using triangular elements that vary in size, the grid achieves fine-scale resolution near the coast, while maintaining coarser resolution offshore.

2.1 Governing equations

The conservation of momentum equations can be written in the form:

$$\begin{aligned} \frac{\partial U_l}{\partial t} + u_l \frac{\partial U_l}{\partial x} + v_l \frac{\partial U_l}{\partial y} + \int_{z_l}^{z_{l-1}} w \frac{\partial u}{\partial z} dz - fV_l \\ = -gh_l \frac{\partial \zeta}{\partial x} - \frac{gh_l}{\rho_0} \int_{H_l}^0 \frac{\partial \rho'}{\partial x} dz \\ - \frac{h_l}{\rho_0} \frac{\partial P_a}{\partial x} + \nabla_h \cdot (A_H \nabla_h U_l) + \int_{z_l}^{z_{l-1}} \frac{\partial \tau_{xz}}{\partial z} dz \end{aligned} \quad (2.1)$$

$$\begin{aligned}
\frac{\partial V_l}{\partial t} + u_l \frac{\partial V_l}{\partial x} + v_l \frac{\partial V_l}{\partial y} + \int_{z_l}^{z_{l-1}} w \frac{\partial v}{\partial z} dz + f U_l \\
= -g h_l \frac{\partial \zeta}{\partial y} - \frac{g h_l}{\rho_0} \int_{H_l}^0 \frac{\partial \rho'}{\partial y} dz \\
- \frac{h_l}{\rho_0} \frac{\partial P_a}{\partial y} + \nabla_h \cdot (A_H \nabla_h V_l) + \int_{z_l}^{z_{l-1}} \frac{\partial \tau_{yz}}{\partial z} dz
\end{aligned} \tag{2.2}$$

Where h_l is the layer thickness, P_a is the atmospheric pressure at the sea surface, g is the gravitational acceleration, ρ_0 is the reference density of sea water, $\rho = \rho_0 + \rho'$ is the water density with ρ' representing the perturbation of the density from the reference value ρ_0 . H_l is the depth of the bottom of layer l , A_H is the horizontal eddy viscosity obtained following the Smagorinsky formulation (Smagorinsky, 1963; Blumberg and Mellor, 1987), w is the vertical layer velocity, f is the Coriolis parameter, $\zeta(x, y, t)$ is the free surface, $l = 1, \dots, N$ is the vertical layer index increasing with depth, $z_l = 0, \dots, N$ are the layer interfaces, u_l is the zonal velocity, v_l is the meridional velocity while U_l and V_l are the horizontal velocity integrated over layer l , and can be defined as:

$$U_l = \int_{z_l}^{z_{l-1}} u_l dz, \quad \text{and} \quad V_l = \int_{z_l}^{z_{l-1}} v_l dz \tag{2.3}$$

The turbulent Reynolds stresses τ_{yz} and τ_{xz} used in (2.1) and (2.2), are defined as:

$$\int_{z_l}^{z_{l-1}} \frac{\partial \tau_{xz}}{\partial z} dz = \tau_{xz}^{z_{l-1}} - \tau_{xz}^{z_l} = A_V \frac{\partial u_l}{\partial z} \tag{2.4}$$

$$\int_{z_l}^{z_{l-1}} \frac{\partial \tau_{yz}}{\partial z} dz = \tau_{yz}^{z_{l-1}} - \tau_{yz}^{z_l} = A_V \frac{\partial v_l}{\partial z} \tag{2.5}$$

Where A_V is the vertical eddy viscosity, calculated with the vertical eddy diffusivity K_V in a two equation model with a $k - \epsilon$ scheme for the turbulence closure, as in the General Ocean Turbulence Model (GOTM) (Burchard et al. ,1999). The turbulent kinetic energy k and turbulent dissipation ϵ are related with A_V and K_V using the Kolmogorov (1941) and Prandtl (1945) relations. At the first and last layers the turbulent Reynolds stresses are obtained by using the surface and bottom boundary conditions of momenta.

The continuity equation for the layer l can be written:

$$\frac{\partial U_l}{\partial x} + \frac{\partial V_l}{\partial y} = w_{z_l} + w_{z_{l-1}} \tag{2.6}$$

The vertically integrated salinity and temperature equations for layer l read respectively:

$$\begin{aligned} \frac{\partial (h_l S_l)}{\partial t} + U_l \frac{\partial S_l}{\partial x} + V_l \frac{\partial S_l}{\partial y} + \int_{z_l}^{z_{l-1}} w \frac{\partial S}{\partial z} dz = \nabla_h \cdot (K_H \nabla_h h_l S_l) \\ + \int_{z_l}^{z_{l-1}} \frac{\partial}{\partial z} \left(K_V \frac{\partial S}{\partial z} \right) dz \end{aligned} \quad (2.7)$$

$$\begin{aligned} \frac{\partial (h_l \theta_l)}{\partial t} + U_l \frac{\partial \theta_l}{\partial x} + V_l \frac{\partial \theta_l}{\partial y} + \int_{z_l}^{z_{l-1}} w \frac{\partial \theta}{\partial z} dz = \nabla_h \cdot (K_H \nabla_h h_l \theta_l) \\ + \int_{z_l}^{z_{l-1}} \frac{\partial}{\partial z} \left(K_V \frac{\partial \theta}{\partial z} \right) dz + \int_{z_l}^{z_{l-1}} \frac{I}{\rho_0 C_p} dz \end{aligned} \quad (2.8)$$

Where S_l and θ_l are respectively the salinity and temperature at layer l , K_H and K_V are respectively the horizontal and vertical turbulent diffusion coefficients, I is the solar irradiance at depth z_l calculated with a double exponential attenuation (Paulson and Simpson, 1977) as below:

$$\frac{I}{I_0} = R \exp -z/\xi_1 + (1 - R) \exp -z/\xi_2 \quad (2.9)$$

In which I_0 is the solar irradiance at the surface (W/m^2) and ξ_1 and ξ_2 are the attenuation lengths corresponding to the absorption of the visible spectrum. The equation of state is necessary to obtain the density ρ , which is computed from salinity temperature and pressure according to UNESCO (United Nations Educational, Scientific and Cultural Organization) as in (Fofonoff and R.C., 1983):

$$\rho_l(x, y, l, t) = \rho_l(S_l, \theta_l, p_l) \quad (2.10)$$

2.2 Boundary conditions

The SHYFEM-MPI model employs a sophisticated set of boundary conditions designed to accurately capture the exchange processes at the limits of its computational domain, ensuring that the simulated dynamics closely reflect real-world coastal processes. At lateral boundaries, tidal forcing is typically imposed through prescribed water levels or elevations that replicate the natural oscillatory behavior observed in coastal environments. These conditions often include radiation boundary formulations, which allow waves and disturbances to exit the domain without excessive reflection, thereby reducing artificial interference with the internal dynamics of the model.

In addition to the lateral boundary conditions, closed boundaries are usually treated as impermeable walls. Depending on the hydrodynamic regime of the area being modeled, either free-slip or no-slip conditions are applied. Free-slip boundaries minimize frictional

effects and are used when simulating flows that are less influenced by bottom friction, whereas no-slip conditions impose a zero-velocity constraint at the boundary to better capture frictional interactions, especially in regions where shear stress is significant. This dual approach allows SHYFEM-MPI to flexibly adapt to various coastal settings, from open estuaries to confined embayments.

Furthermore, the model incorporates specialized boundary conditions at river inlets and estuarine interfaces, where freshwater fluxes play a critical role. These conditions account for variations in river discharge, salinity, and sediment load, providing a realistic representation of the mixing processes between freshwater and seawater. Such detailed treatment is essential for capturing the stratification and circulation patterns that can be heavily influenced by river inputs, which in turn affect nutrient transport and ecological dynamics.

Bottom Boundary Condition and Drag Formulation

At the bottom boundary, SHYFEM-MPI typically uses a friction law to represent the shear stress exerted by the bed on the flow. The standard formulation for the bottom shear stress is given by

$$\tau_b = \rho C_d |\mathbf{u}_b| \mathbf{u}_b,$$

where ρ is the water density, C_d is the bottom drag coefficient, \mathbf{u}_b is the near-bottom velocity vector.

This formulation accounts for the momentum loss due to friction between the water and the seabed.

In coastal areas where seagrass meadows are present, the drag induced by vegetation significantly enhances the overall bottom friction. Seagrasses increase the effective roughness of the seabed by introducing additional drag forces. This vegetation-induced drag can be represented by an additional term in the drag equation:

$$\tau_{sg} = \rho C_{D,sg} a |\mathbf{u}_b| \mathbf{u}_b,$$

where: $C_{D,sg}$ is the seagrass drag coefficient, a is the frontal area density (area of seagrass blades per unit volume).

This formulation captures the effect of seagrass on reducing current velocity and enhancing turbulent mixing, as the increased drag leads to greater momentum dissipation. The combination of the standard bottom shear stress and the additional seagrass-induced drag provides a comprehensive description of the frictional forces at the seafloor, particularly in shallow coastal environments where seagrass is abundant.

Overall, the boundary condition framework within the SHYFEM-MPI model is integral to its performance, ensuring that tidal dynamics, freshwater inputs, and coastal interactions are modeled with high fidelity. By combining realistic open-boundary forcing, adaptable lateral boundary treatments, specialized conditions for riverine inputs, and a detailed formulation of the bottom boundary condition—including the enhanced

drag effects due to seagrass—the model offers a robust tool for investigating complex coastal hydrodynamics and environmental processes.

Chapter 3

Model setup

3.1 Domain of simulation

The horizontal discretization of the area has an increasing resolution from 2.2 km offshore, the same as the unstructured parent model, to a nearshore resolution of around 300 m at the coast. In figure 3.1 the SHYFEM-MPI horizontal domain is represented with the seagrass distribution. The main advantage of adopting an unstructured grid is the flexibility to represent irregular coastlines, while also allowing for less expensive computations. The finer resolution near the coastline also allows for a more accurate representation of shallow water processes, which are crucial for understanding interactions between seagrass meadows and hydrodynamics. The vertical grid is composed of 42 layers in zeta coordinates, with layers 1 m thick.

The analysis presented in Chapter 4 and 5 focuses on a refined horizontal grid, selected using latitude and longitude to better investigate the impact of seagrass elements. This subdomain, visible in figure 3.2, extends along the coast covering the area from Porto Garibaldi to Marina di Ravenna. This spatial refinement allows for a more detailed examination of localized hydrodynamic and ecological interactions influenced by seagrass presence.

A number of locations were chosen by hand, selecting which grid elements would have seagrass in them. The seagrass elements are distributed on the unstructured SHYFEM-MPI grid in sparse order, mimicking the actual presence of *Zostera Marina* on the Adriatic coast (B. Ondiviela et al., 2013). The horizontal distribution of seagrass is the same for each scenario and is constant over time, ensuring that differences in the simulation outcomes are solely due to variations in the parameterized seagrass characteristics.

The grid elements within the domain that were assigned the presence of seagrass are represented in Figure 3.1 as green triangles, visible in the inset on the right-hand side of the image. This inset highlights a refined portion of the mesh, illustrating the spatial distribution of seagrass across the coastal region, particularly along the Adriatic Sea near

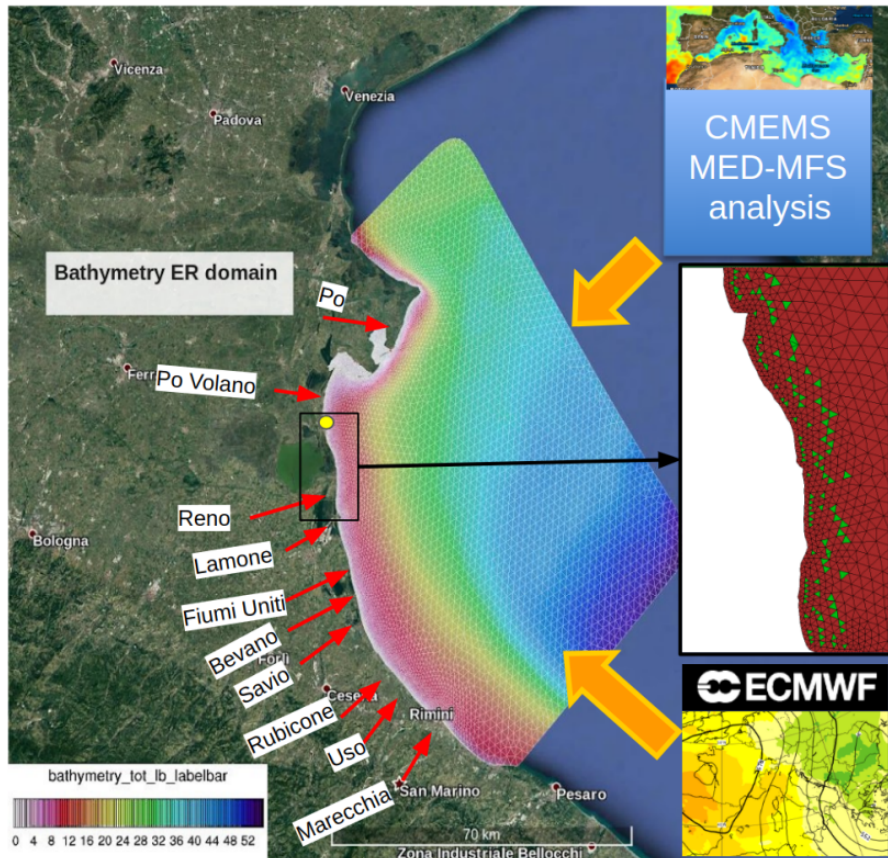


Figure 3.1: SHYFEM-MPI simulation domain and seagrass implementation, this image was taken from J. Alessandri "COASTAL MODELLING STUDIES FOR FORECASTING AND REMEDIATION SOLUTIONS, 2021"

the Emilia-Romagna coast, between Porto Garibaldi and Marina di Ravenna.

3.1.1 Parameter Selection and Variability

A "What If Scenario" (WiS) is a structured approach used in modeling to investigate the effects of varying key parameters on system behavior. By deliberately altering these parameters within a plausible range, WiS allows researchers to simulate hypothetical conditions and assess the sensitivity of the system to changes. This method is instrumental in exploring alternative futures, evaluating management strategies, or understanding potential responses of the system to environmental changes. In essence, each WiS represents a unique combination of parameter values that can reveal how variations in those parameters might influence the overall dynamics, offering valuable insights into the resilience and adaptability of the system under study (Tagliapietra et al., 2009).

Implementation of seagrass in the SHYFEM-MPI model was achieved by incorporat-

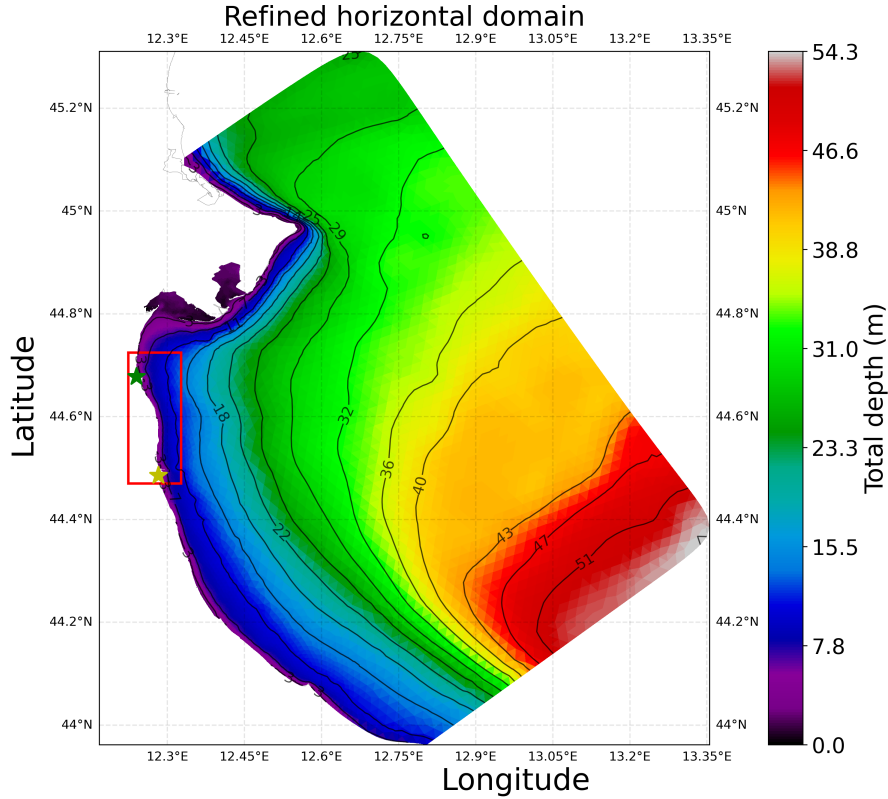


Figure 3.2: Bathymetric map of the SHYFEM-MPI domain with a refined horizontal grid along the coast, illustrating total depth (m) of grid elements. The red rectangle highlights the subdomain of interest, with yellow and green stars marking key reference points.

ing three key parameters at the patch level: plant shoot number density, leaf length, and leaf width. To account for the natural variability observed in Adriatic coastal waters, three representative values were chosen for each parameter. This systematic variation resulted in a total of 27 unique What If Scenarios (WiS), each representing a different combination of seagrass characteristics. These WiS enable the model to simulate a wide range of potential seagrass effects on coastal hydrodynamics. The outcomes from these scenarios provide a detailed understanding of how changes in seagrass morphology can affect water circulation, sediment transport, and overall ecological dynamics. The parameters selected for each WiS are summarized in Table 1, offering a comprehensive overview of the variability in seagrass properties and their corresponding hydrodynamic impacts.

The values for N_v , L_v , and B_v were derived from empirical data on seagrass species in the Adriatic and Mediterranean regions, as documented in the literature (see Table 3.3). For N_v , shoot densities of 230, 500, and 960 shoots/m² were selected, reflecting the range observed for *Zostera marina* (e.g., 63–962 shoots/m², Guidetti et al., 2001; Danovaro

Table of the Experiments		L_v (cm)		
N_v (n. shoot / m ²)	b_v (cm)	2	30	60
230	0.2	Wis-1	Wis-10	Wis-19
	0.6	Wis-2	Wis-11	Wis-20
	1.0	Wis-3	Wis-12	Wis-21
500	0.2	Wis-4	Wis-13	Wis-22
	0.6	Wis-5	Wis-14	Wis-23
	1.0	Wis-6	Wis-15	Wis-24
960	0.2	Wis-7	Wis-16	Wis-25
	0.6	Wis-8	Wis-17	Wis-26
	1.0	Wis-9	Wis-18	Wis-27

Figure 3.3: Range of seagrass phenological characteristics used to produce "What If" scenario simulations

et al., 2020) and *Posidonia oceanica* (e.g., 475.7–773.1 shoots/m², Guidetti et al., 2001; Macic, 2001). For leaf length (L_v), values of 2 cm, 30 cm, and 60 cm were chosen, encompassing the typical range for *Zostera marina* (15.2–27.5 cm, Guidetti et al., 2001) and *Posidonia oceanica* (13–78.4 cm, Guidetti et al., 2001; Macic, 2001). Similarly, leaf widths (B_v) of 0.2 cm, 0.6 cm, and 1.0 cm were selected, aligning with the observed variability for *Zostera marina* (0.26–0.5 cm, Mazzella et al., 1998) and *Posidonia oceanica* (0.4–1.2 cm, Mazzella et al., 1998; Borum et al., 2004).

These parameter ranges were chosen to reflect seasonal and species-specific differences, such as winter versus summer growth patterns and juvenile versus adult stages, as reported in the references (e.g., Guidetti et al., 2001; Mazzella et al., 1998). The resulting 27 WiS experiments (e.g., Wis-1 to Wis-27) allowed for a systematic evaluation of how seagrass density, length, and width influence hydrodynamic processes, including current velocity, turbulence, and sediment dynamics, within the refined coastal grid of the SHYFEM-MPI domain (as shown in Figure 3.1).

The flexibility of leaves was implemented in the model by defining a modified drag formulation. Following Luhar and Nepf (2011), a flexibility parameter is introduced that effectively reduces C_d to an effective drag coefficient $C_{d,\text{eff}}$, expressed as:

$$C_{d,\text{eff}} = C_d \left(1 - \alpha \frac{U}{U_{\text{ref}}} \right),$$

where α is a dimensionless parameter representing the degree of flexibility and U_{ref} is a reference velocity scale. This formulation captures the reconfiguration of seagrass leaves under increasing flow, thereby reducing the net drag and altering the local turbulence characteristics. The introduction of seagrass not only affects momentum through drag modification but may also influence turbulent mixing and sediment transport. The reduced drag from flexible leaves can lead to localized changes in turbulent kinetic energy (TKE), potentially impacting nutrient cycling and sediment resuspension (Duarte et al., 2013).

Future extensions of this work might incorporate dynamic vegetation responses, allowing for seasonal variations or growth–decay cycles, thereby providing a more comprehensive picture of seagrass-ecosystem interactions.

3.2 Simulation setup

The simulation is conducted over a one-year period from January 1, 2020, to December 31, 2020, focusing on the northern Adriatic Sea. Temporal resolution is maintained at an hourly timestep, ensuring that both diurnal variations (such as tidal oscillations) and seasonal trends are adequately resolved. In our model implementation, a variety of boundary conditions are employed to ensure that the simulation accurately reflects both local and regional forcing. The atmospheric forcing is derived from the European Centre for Medium-Range Weather Forecasts (ECMWF) dataset, which provides high-resolution, globally consistent wind, temperature, humidity, and pressure fields. These data drive the air–sea fluxes in the model, ensuring that the surface stress and heat exchanges are representative of observed atmospheric conditions.

For the oceanic boundaries, we use data from the Copernicus program (Clementi et al., 2017) from the Mediterranean Monitoring Forecasting Centre (MED MFC). This source supplies the necessary sea surface height, temperature, and salinity fields at the open boundaries of our domain. The use of COPERNICUS MED data ensures that the lateral boundary conditions reflect realistic regional ocean dynamics, including tidal influences and mesoscale variability, which are critical for accurately modeling the coastal circulation.

Riverine inputs are handled with special consideration due to their significant impact on local hydrography. For the Po River, which is a major freshwater source in the study area, we employ boundary conditions based on high-quality measurements from ARPAE. These data capture the temporal variability and magnitude of the Po River discharge with high fidelity. For all other rivers, a 30-year climatology is utilized to define the inflow conditions. This long-term average approach helps to smooth out short-term fluctuations and provides a robust estimate of the typical freshwater contributions from these smaller catchments.

3.3 Datasets

Each "What if Scenario" simulation outputs a diverse array of physical variables critical for understanding coastal dynamics. Key outputs include sea surface elevation, the zonal and meridional velocity components, and the temperature and salinity profiles across the vertical layers. Each simulation is stored as an hourly dataset in NetCDF format, which supports efficient data handling and facilitates integration with post-processing tools.

In addition to the 27 seagrass scenarios, a control dataset was generated using the same numerical setup but without incorporating seagrass effects. This control simulation provides a baseline against which the influence of seagrass on coastal hydrodynamics can be robustly compared. The dataset is systematically organized to allow for both spatial and temporal analyses: raw data are available at full resolution, and derived products—such as vertical integrals, spatial averages, and statistical metrics—are generated during post-processing.

3.4 Method of analysis

To complement the analysis of hydrodynamic and scalar fields, we compute key statistical properties of the model outputs. For any variable $x(t)$, the arithmetic mean μ and standard deviation σ are computed as:

$$\mu = \frac{1}{N} \sum_{i=1}^N x(t_i), \quad \sigma = \sqrt{\frac{1}{N} \sum_{i=1}^N (x(t_i) - \mu)^2},$$

where N represents the total number of time steps.

The first phase of our analysis focuses on characterizing the regional properties of the control simulation, which excludes seagrass. We begin by calculating the overall mean salinity and temperature across the basin by averaging over the horizontal and vertical dimensions, to capture the temporal evolution of these key variables. To delve deeper into the vertical structure, we generate time series for each layer's horizontal average, allowing us to track how temperature and salinity change throughout the water column during the year. In addition, we create a series of maps that illustrate the time-integrated distributions of temperature and salinity from the bottom layer to the surface, complemented by analyses of their temporal variability using standard deviation measures.

Next, we apply the same approach to the scenario with the highest seagrass parametrization. This direct comparison between the control and seagrass scenarios enables us to isolate and assess the impact of seagrass on the basin's thermal and saline structure.

In the second phase of our analysis, we shift our attention to the influence of seagrass on current velocity. We start by examining the time series of both the magnitude and the

direction of the current at each vertical layer in the same way it was done for temperature and salinity. With these insights, we then construct horizontal maps that display the time averaged currents in the region at specific layers. Finally, a spectral analysis is performed to estimate the power spectral density (PSD) of the speed magnitude at specific frequencies. The PSD, $P_{xx}(f)$, is given by:

$$P_{xx}(f) = \frac{1}{K} \sum_{k=1}^K |X_k(f)|^2,$$

where $X_k(f)$ is the Fourier transform of the k -th segment of the time series and K is the number of segments. This method helps to reveal the dominant frequency components and energy distribution in the flow, which are essential for understanding the modifications induced by seagrass presence.

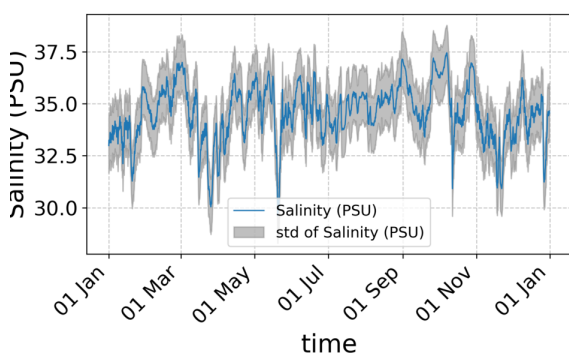
Chapter 4

Analysis

4.1 Control Characterization

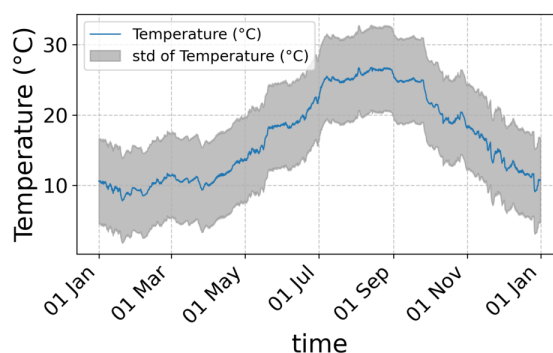
The control analysis focuses on the integrated properties of the region of interest described in section 3.1 . In Figure 4.1 (left panel), we display the time series of basin-integrated salinity . This variable is computed by vertically integrating each element by using the layer thicknesses and horizontally integrated weighting each element by its area and element-wise standard deviation. The mean hourly salinity is around 33 psu for most of the year, with minima of approximately 30 psu during periods of high river runoff and peaks reaching up to 36 psu when evaporation is dominant.

Time series of integrated Salinity (PSU)



(a) Basin-integrated salinity time series.

Time series of integrated Temperature (°C)



(b) Basin-integrated temperature time series.

Figure 4.1: Integrated time series of (a) salinity and (b) temperature with their spatial standard deviations.

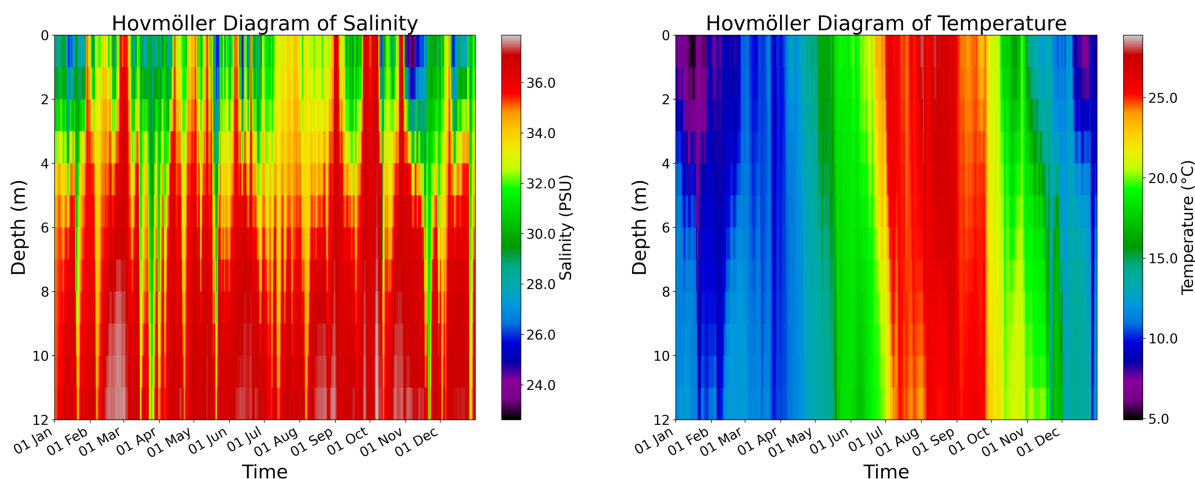
The standard deviation associated with the average salinity time series quantifies the horizontal variability at each time step. In particular, intense precipitation events significantly affect both the mean salinity and its variability. Multiple river outflows in

the region further contribute to reducing salinity throughout the year, producing local minima between 25 psu and 30 psu at different times, while occasional peaks reach up to 38 psu in autumn and spring.

Figure 4.1 (right panel) shows the integrated temperature time series, which exhibit a strong seasonal dependence with higher spatial variability during the warmer months: the mean water temperature ranges from approximately 10 °C in winter to 25 °C in summer, with a variability of around 10 °C.

4.1.1 Vertical Profiles (Hovmöller Diagrams)

The vertical profiles of temperature and salinity are analyzed by computing their horizontal average at each time interval, weighting each element with its area. In the Hovmöller diagrams 4.2, the vertical axis represents depth (from the bottom to the surface) and the horizontal axis represents time. The color scale indicates the integrated salinity (in units of psu) or integrated temperature (in °C), with blue for lower values and red for higher values.



(a) Hovmöller diagram of integrated salinity. (b) Hovmöller diagram of integrated temperature.

Figure 4.2: Hovmöller diagrams of horizontally averaged integrated (a) salinity and (b) temperature.

These diagrams illustrate how freshwater inputs at the surface reduce salinity even at lower depths during periods of high precipitation or riverine discharge. Since density increases with salinity, fresher surface waters remain less dense, while deeper layers stay more saline and denser. Consequently, in summer, stratification is stronger, with warmer, less dense water above colder, denser layers. During winter, while surface cooling tends to increase the density of the upper layer, salinity differences continue to dictate the density structure and, consequently, the vertical stratification of the water column.

4.1.2 Vertical Profiles of Speed

Figure 4.3 displays the vertical profile of the horizontally integrated speed magnitude. The vertical axis indicates depth (from the bottom to the surface) and the horizontal axis represents time. The color scale indicates increasing flow intensity in units of cm/s , highlighting the temporal evolution of the flow field across the water column. It is evident that the highest velocities are reached in the surface layer, with occasional events influencing the entire water column. At the deepest layers, current speed does not generally exceed 5 cm/s on a yearly average, while at the surface layer, values upwards of 15 cm/s seem to be common.

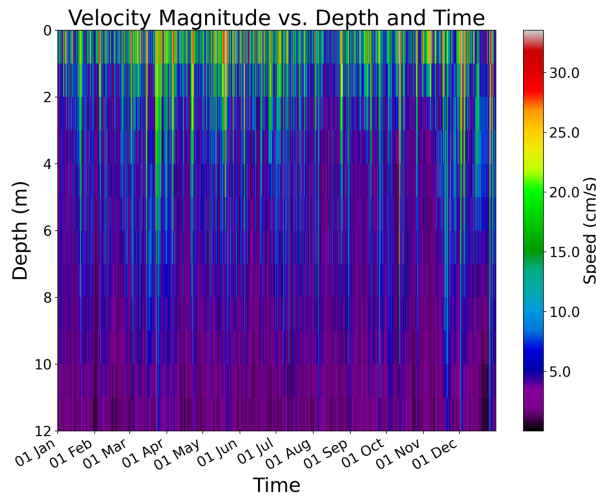


Figure 4.3: Hovmöller diagram of integrated speed magnitude.

4.1.3 Horizontal Maps at Surface and Bottom Layers

The following analysis examines the spatial distribution of temperature, salinity, and speed magnitude at both the surface and bottom layers. Each map includes time-averaged local current directions (in degrees) depicted by black arrows. The coastline is extracted from the EMODnet bathymetry dataset (EMODnet Bathymetry Consortium, 2020) at 10 m in resolution (drawn in gray), and the cities of Porto Garibaldi and Marina di Ravenna are marked with a green star and a yellow star, respectively.

Velocity Maps Figure 4.4 shows the control dataset's time-averaged velocity magnitude for the surface (left) and bottom (right) layers. The x- and y-axes represent longitude and latitude, and the color scale indicates current speed in cm/s . Surface currents display high speeds near the major riverine outflow of the Reno river (up to 26 cm/s). In the Marina di Ravenna harbor, surface speeds are particularly low, while

outside of it the surface speed increases due to interactions with the wall of the harbor. At the bottom layer, currents exhibit generally lower speed with localized regions near river mouths reaching about 10 cm/s.

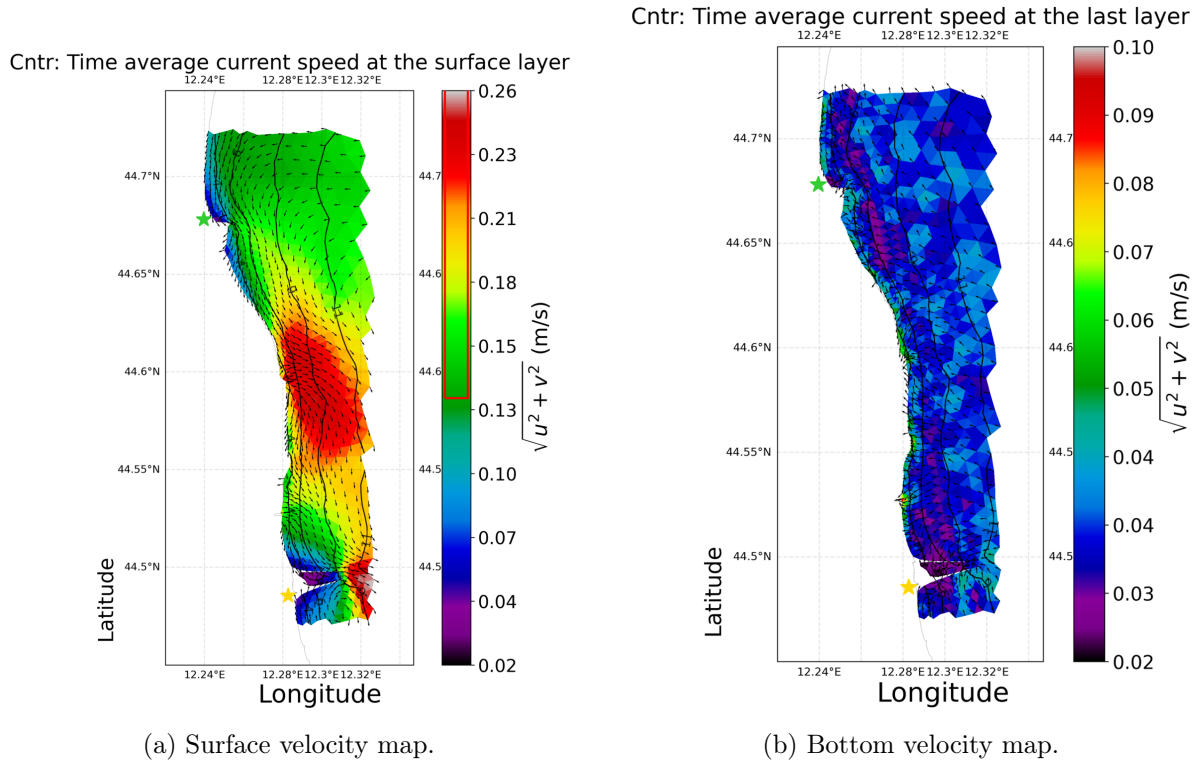
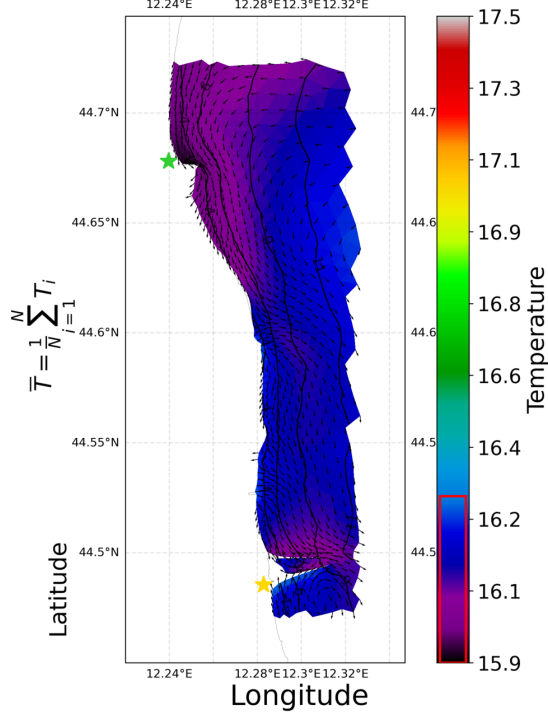


Figure 4.4: Time-averaged velocity magnitude maps for the control case: (a) surface layer and (b) bottom layer.

Temperature Maps Figure 4.5 presents the time-averaged temperature fields for the surface (left panel) and bottom (right panel) layers. The yearly averaged data reveal that the vertical stability of the water column is maintained primarily by the salinity vertical profile. While temperature differences are present, the dominant factor governing stratification is the salinity gradient: freshwater inputs reduce surface salinity, resulting in less dense water at the top, whereas deeper layers retain higher salinity and thus greater density. This salinity-driven density structure ensures a stable vertical stratification over the annual cycle.

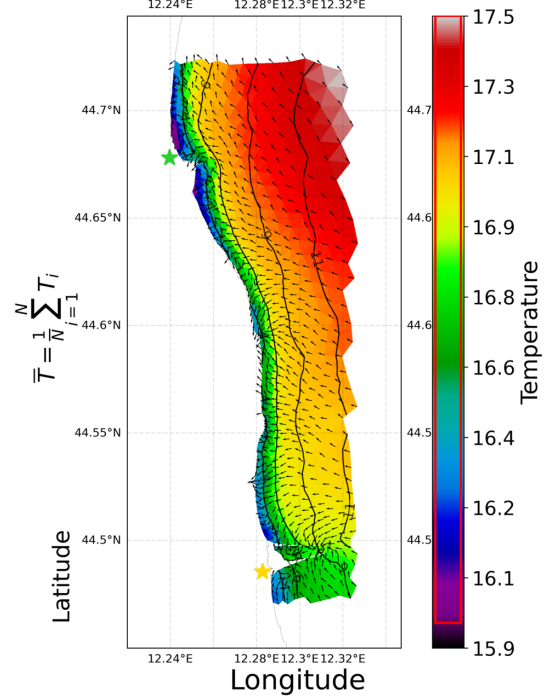
Potential Density The potential density was calculated using the TEOS-10 formulation (McDougall et al., 2013) to assess the stability of the water column. This approach computes in-situ density from measured practical salinity and temperature by first con-

Cntr: Time average temperature at the surface



(a) Surface temperature map.

Cntr: Time average temperature at the last layer



(b) Bottom temperature map.

Figure 4.5: Time-averaged temperature maps for the control case: (a) surface layer and (b) bottom layer.

verting these to Absolute Salinity (SA) and Conservative Temperature (CT) and then evaluating the density via the partial derivative of the specific Gibbs function.

By examining figure 4.7, we can identify regions with significant stratification that are likely to exhibit limited vertical mixing. This variable was analyzed to guarantee the stability of higher temperature water at the last layer, with respect to the surface layer, as seen from the temperature maps.

Salinity Maps Figure 4.8 presents the time-averaged salinity for the surface (left) and bottom (right) layers. The maps show pronounced gradients near river mouths, with higher salinity values offshore and in deeper layers due to stratification.

Sea Surface Height Map Figure 4.9 shows the time averaged sea surface height map. The effect of the Reno river on the sea surface height can be seen as a red spot in the center of the map. In the north and in the south of the region, the current direction lines suggest that a higher sea surface height may be explained by water accumulation against a solid barrier, respectively the Bellocchio beach, and the coast north of Marina

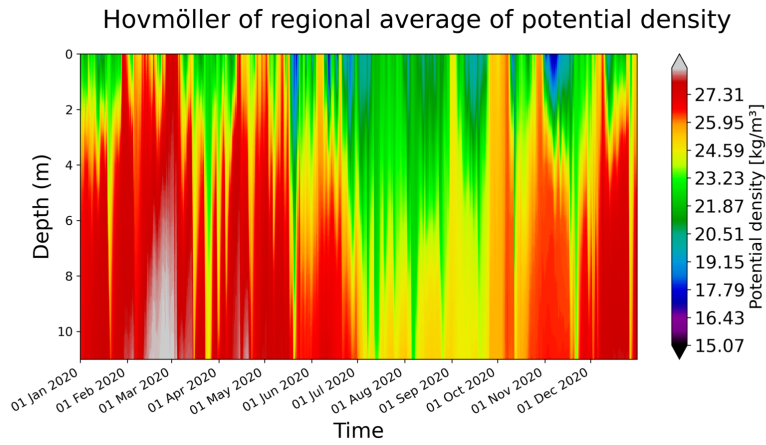


Figure 4.6: Vertical distribution of potential density time series (kg/m^3) for the control run, calculated at 0 dbar using the TEOS-10 formulation.

Cntr: Time-averaged potential density difference (last layer - surface)

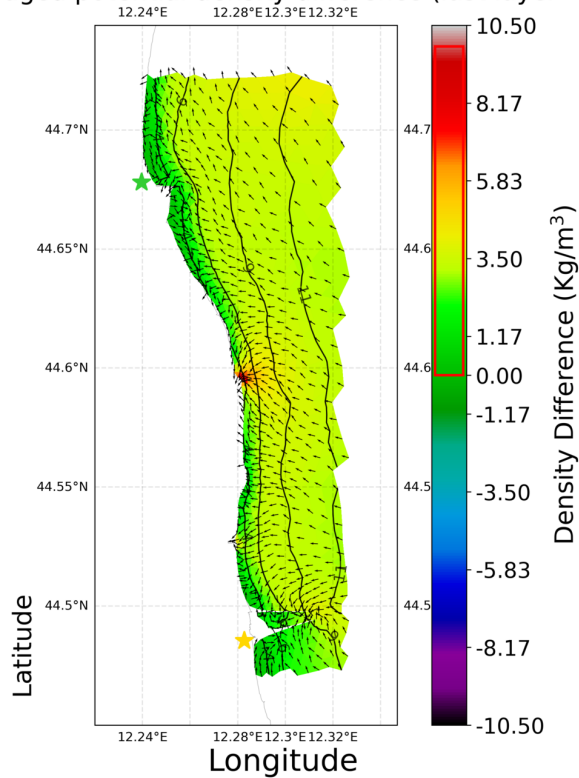
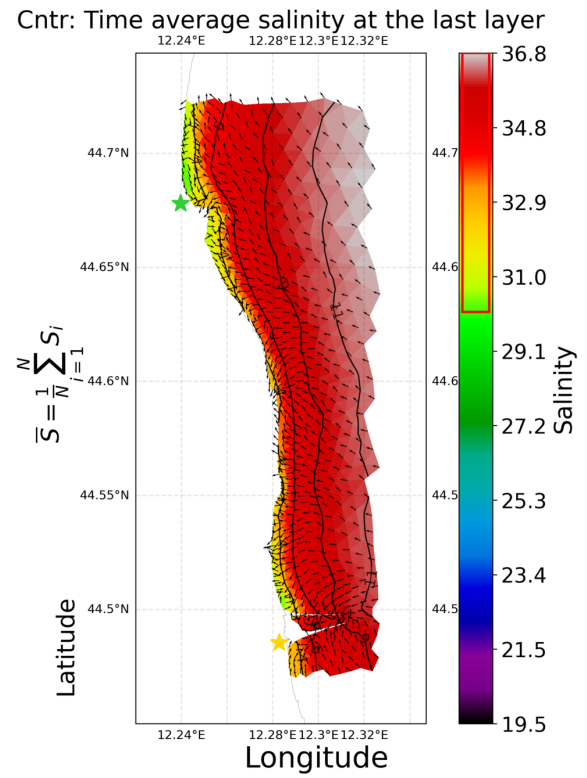
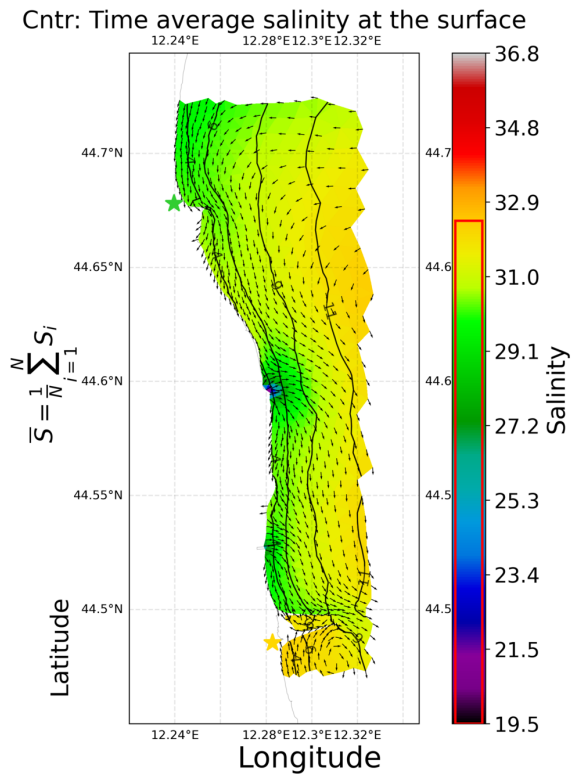


Figure 4.7: Spatial distribution of potential density (kg/m^3) difference between last layer and the surface for the control run, calculated at 0 dbar using the TEOS-10 formulation.



(a) Surface salinity map.

(b) Bottom salinity map.

Figure 4.8: Time-averaged salinity maps for the control case: (a) surface layer and (b) bottom layer.

di Ravenna harbor.

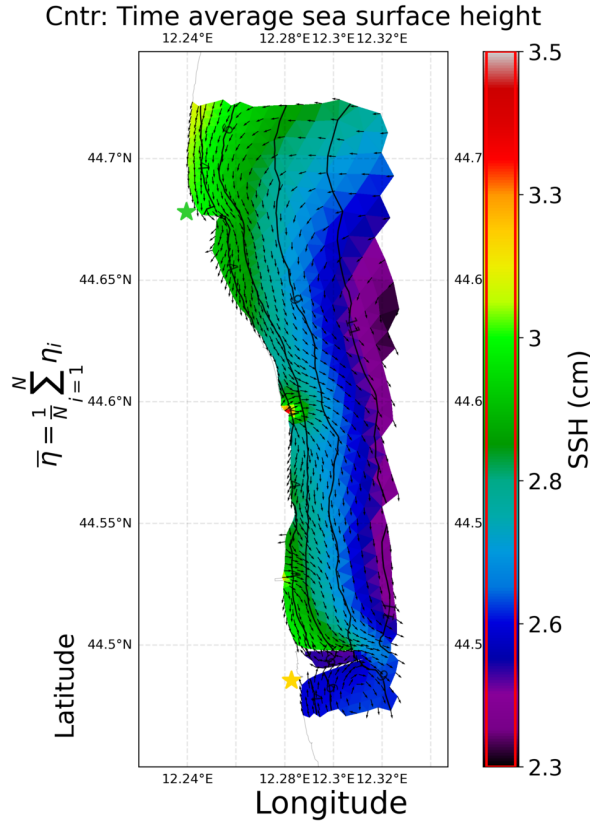


Figure 4.9: Sea surface height time average map (*cm*).

Spectral Maps

Spectral analysis of the current velocity time series was conducted using Welch’s method (Welch P., 1967) , which provides robust estimates of the power spectral density. We selected three representative points within the region of interest and computed their respective power spectra to analyze the dominant periodic components of the current velocity. By examining the spectral plots, we observed that all three locations exhibited pronounced intensity peaks at 12-hour and 24-hour periods. These peaks indicate the presence of strong semidiurnal and diurnal tidal components across the study area. Given their consistent dominance in the spectra at all selected points, we focused our analysis on these two periodicities to better understand the hydrodynamic system (see Figure 4.10).

Figures 4.11 and 4.12 display the spectral transformation intensity maps of current velocity for the control case at periods of 12 h and 24 h, respectively. The x- and y-axes indicate longitude and latitude, and the color scale represents the spectral intensity relative to the maximum value observed. The results indicate that the energy is predominantly concentrated at 24 hours, suggesting a stronger influence of diurnal tidal

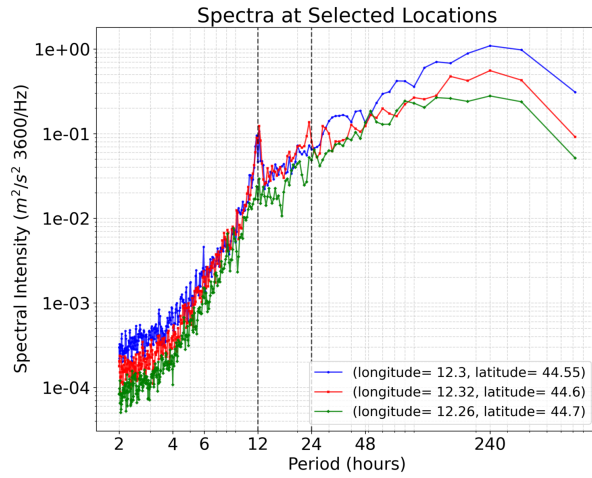
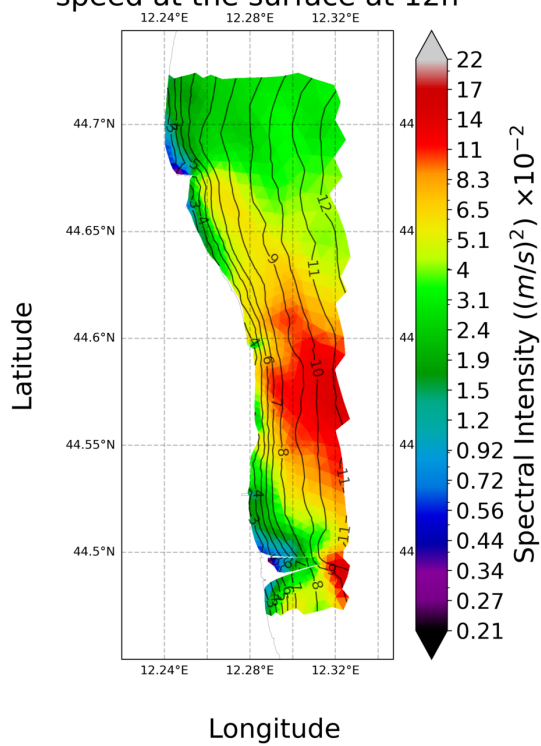


Figure 4.10: Spectral intensity maps at three selected locations. The intensity peaks at 12 h and 24 h highlight the dominant semidiurnal and diurnal variability in the current velocity.

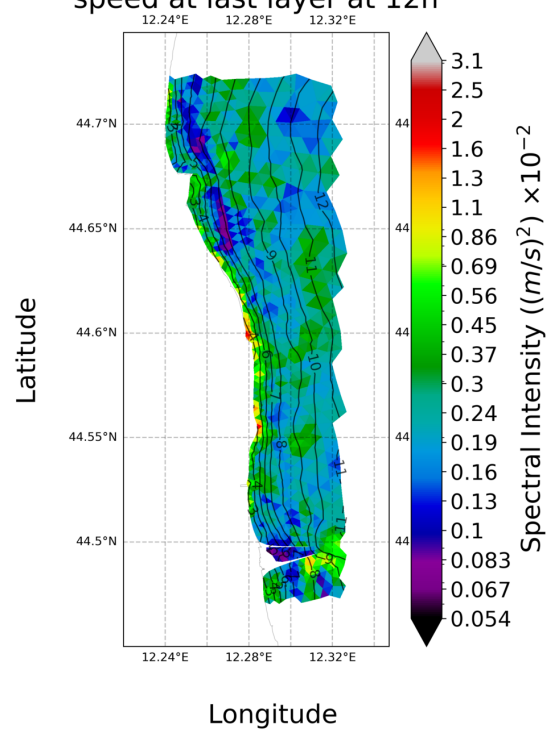
components compared to semi-diurnal ones. At the surface, the spectral intensity is notably higher and more localized, especially in the central and southern areas, while at the bottom it is weaker and more diffuse, likely due to frictional damping. The spatial variability observed across the domain underscores the importance of bathymetric features and coastline geometry in modulating the flow, with daily tidal cycles emerging as the primary driver of the overall energy distribution.

Cntr spectral intensity map of current speed at the surface at 12h



(a) Surface spectral map (12 h).

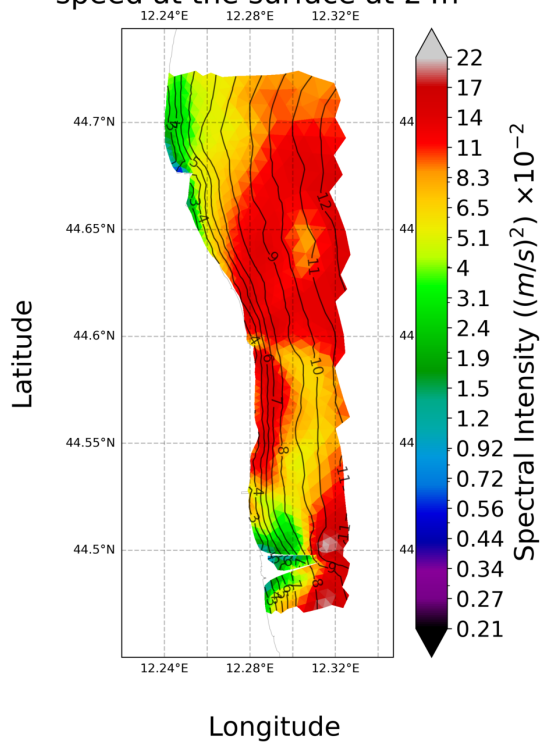
Cntr spectral intensity map of current speed at last layer at 12h



(b) Bottom spectral map (12 h).

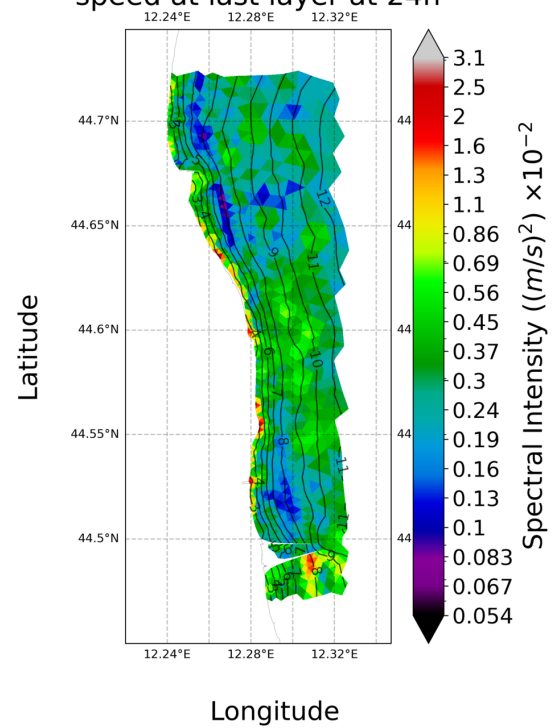
Figure 4.11: Spectral transformation intensity maps for the control case at 12 h: (a) surface layer and (b) bottom layer.

Cntr spectral intensity map of current speed at the surface at 24h



(a) Surface spectral map (24 h).

Cntr spectral intensity map of current speed at last layer at 24h



(b) Bottom spectral map (24 h).

Figure 4.12: Spectral transformation intensity maps for the control case at 24 h: (a) surface layer and (b) bottom layer.

4.2 Seagrass Scenario Characterization

In this section, we analyze the effect of the seagrass parametrization model “WiS-27” as presented in Table 3.3 over the restricted region of interest described in section 3.1 . The analysis is conducted by presenting the seagrass-only variables and successively its differences with the control model, which are computed as "WiS-27" minus Control. This seagrass configuration, characterized by the maximum values for all three parameters, which are leaf length of 60 cm, leaf width of 1 cm, and a surface leaf density of 960 m^{-2} , is expected to induce the most significant differences relative to the control case. The elevated values amplify the drag exerted by the seagrass canopy, resulting in a more pronounced reduction in current velocity and alterations in turbulence and sediment transport processes. Consequently, WiS-27 serves as an extreme scenario that highlights the potential impact of dense and well-developed seagrass meadows on coastal hydrodynamics.

Basin-Averaged Salinity and Temperature

Figure 4.13 illustrates the basin-averaged salinity and temperature. Here, the abscissas represent time in hourly values and the ordinates show the spatially averaged variables. The standard deviation here is calculated over restricted domain. As we can see, the seagrass slightly influences the water column by modifying local mixing and stratification, resulting in very small variations in the basin-wide averages.

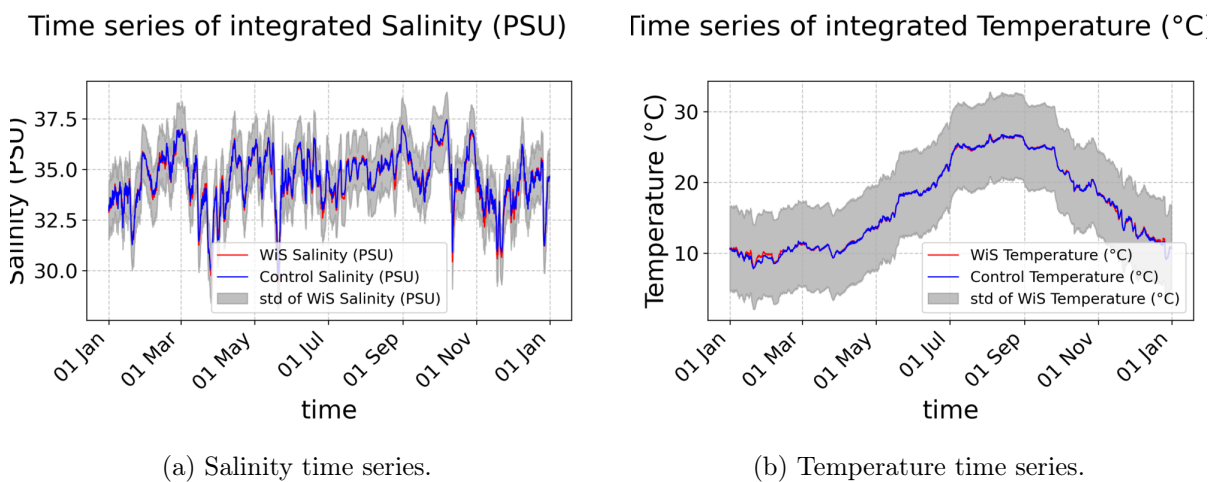
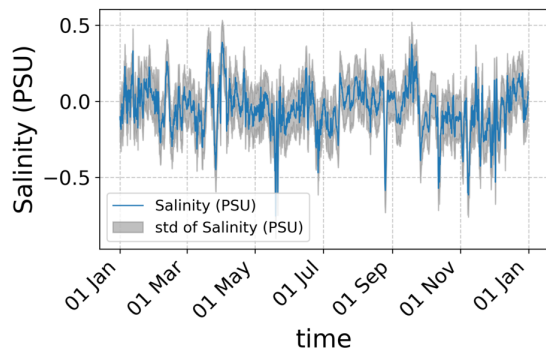


Figure 4.13: Regional average of salinity (left) and temperature (right) time series for the seagrass model.

Figure 4.14 shows the horizontal and vertical averages of salinity and temperature obtained by subtracting the Control model from the seagrass scenario. The abscissas

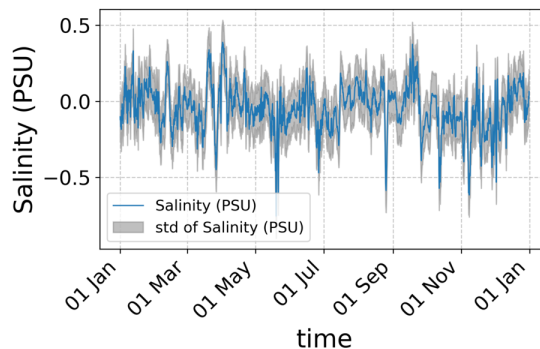
represent time in hourly values, while the ordinates indicate the spatially averaged salinity and temperature. It can be seen that seagrass has little effect on basin integrated salinity and temperature, with small differences due to the altered dynamics.

Time series of integrated Salinity (PSU)



(a) Salinity time series.

Time series of integrated Salinity (PSU)



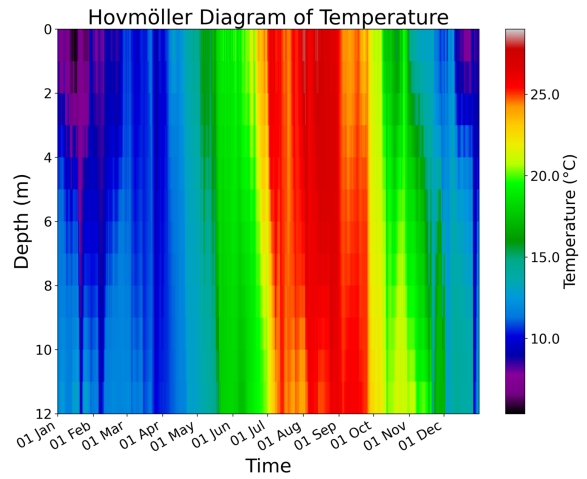
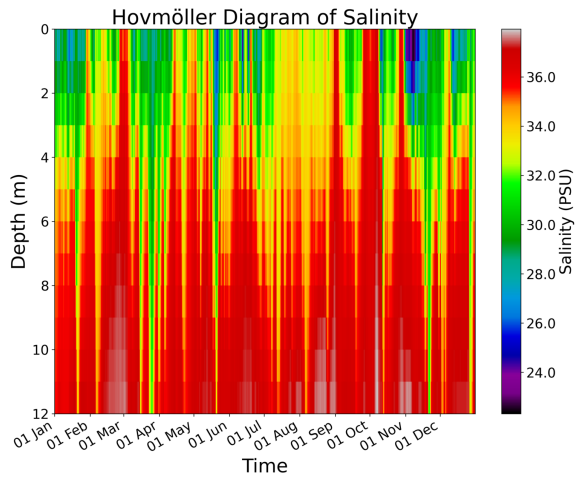
(b) Temperature time series.

Figure 4.14: Regional average of salinity (left) and temperature (right) time series for the difference (seagrass minus control).

Hovmöller Diagrams of Temperature and Salinity

Figure 4.15 presents the Hovmöller diagrams for the "WiS-27" model. These diagrams display horizontally averaged vertical profiles of temperature and salinity, with depth (from bottom to surface) on the vertical axis and time on the horizontal axis. The salinity shows consistently higher values at the bottom layer, like in the control model, with higher variation at the surface layer. A few events of complete vertical mixing are visible, corresponding to the ones observed for the control scenario.

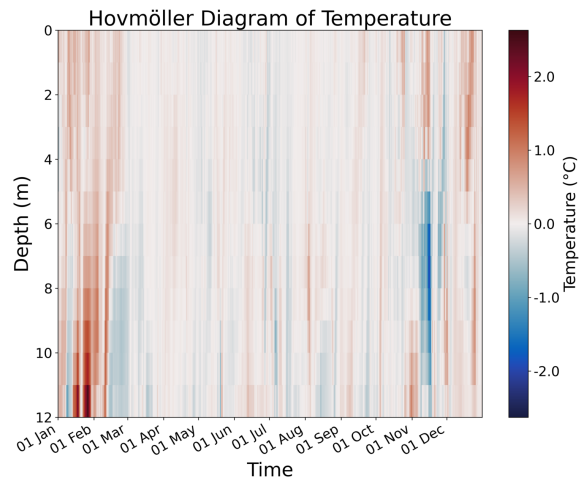
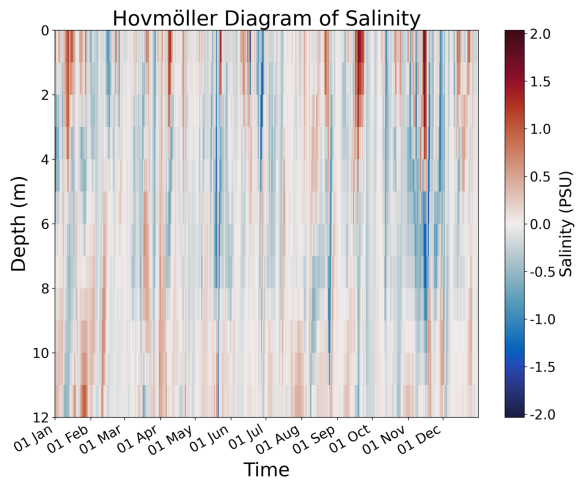
In figure 4.16 the horizontally averaged vertical profiles of temperature and salinity are shown for the difference "WiS-27" minus Control. We can see that during periods of intense river runoff the influx of freshwater enhances vertical stratification, causing the Control model to exhibit relatively higher salinity at depth compared to the seagrass scenario. Surface differences of salinity are also observed, indicating higher values in the seagrass model, which may be attributable to differences in the water dynamics near the coast, as can be seen in the next section of the analysis. Overall the vertical analysis reveal that the presence of seagrass alters vertical mixing patterns, particularly in regions where the vegetation modifies local turbulence and stratification.



(a) Hovmöller diagram of integrated salinity.

(b) Hovmöller diagram of integrated temperature.

Figure 4.15: Hovmöller diagrams for the seagrass model.



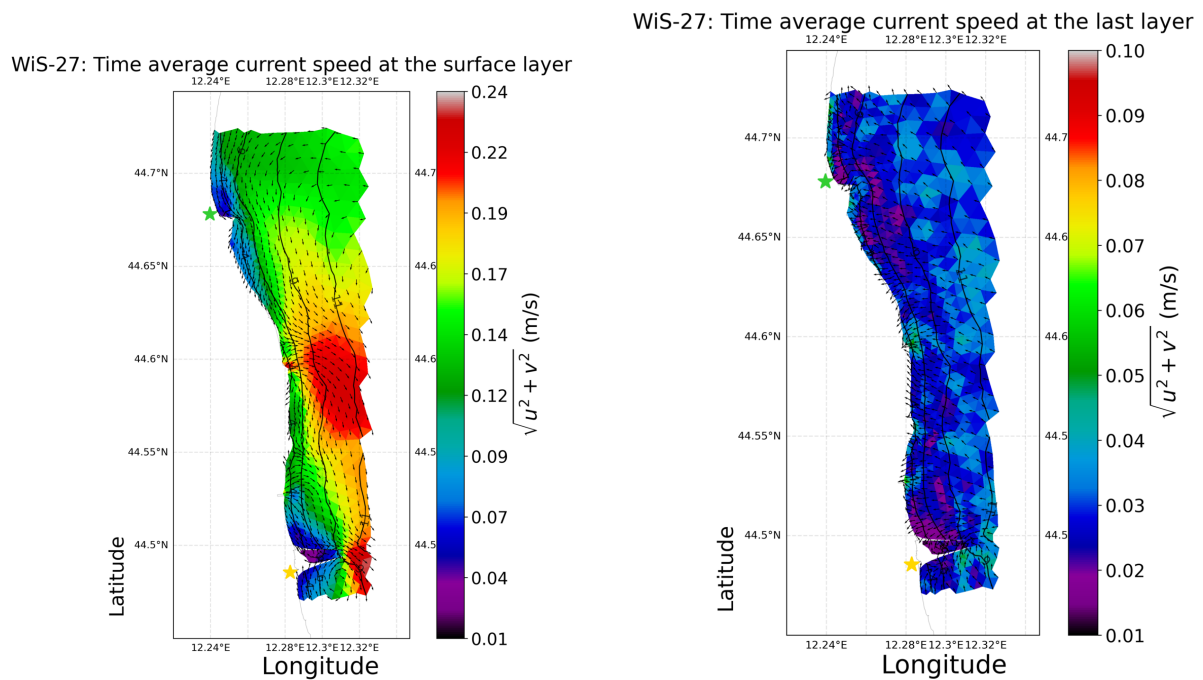
(a) Hovmöller diagram of integrated salinity.

(b) Hovmöller diagram of integrated temperature.

Figure 4.16: Hovmöller diagrams for the difference (seagrass minus control).

Maps of Surface and Bottom Layer Properties

Velocity Figure 4.17 presents the time-averaged velocity magnitude maps for the "WiS-27" scenario, highlighting the difference between the seagrass and control conditions at both the surface and the last (bottom) layer. The black arrows on the map indicate the local current directions, showing a general flow pattern influenced by the coastal and riverine dynamics in the region. At the surface, the current velocity is highest near the major riverine outputs, where velocities reach up to 24 cm/s. In contrast, the last layer shows significantly lower velocities, with the highest values reaching about 8 cm/s, suggesting a reduction in flow speed near the seabed. The interaction with the flow appears to be most pronounced where seagrass is present at shallower depths, likely due to increased turbulence generation above the canopy.



(a) Surface layer velocity map.

(b) Bottom layer velocity map.

Figure 4.17: Time-averaged velocity magnitude maps for the seagrass model.

Figure 4.18 illustrates the time-averaged velocity magnitude maps for the difference between the seagrass scenario and the Control model. At the surface, pronounced differences are observed, especially near river mouths, where the current speed significantly decreases with the adoption of this seagrass parametrization. At the bottom the differences are more localized to areas with seagrass coverage: the current velocity is reduced in the grid elements where seagrass is present, because of the increased turbulence production and the increased drag force.

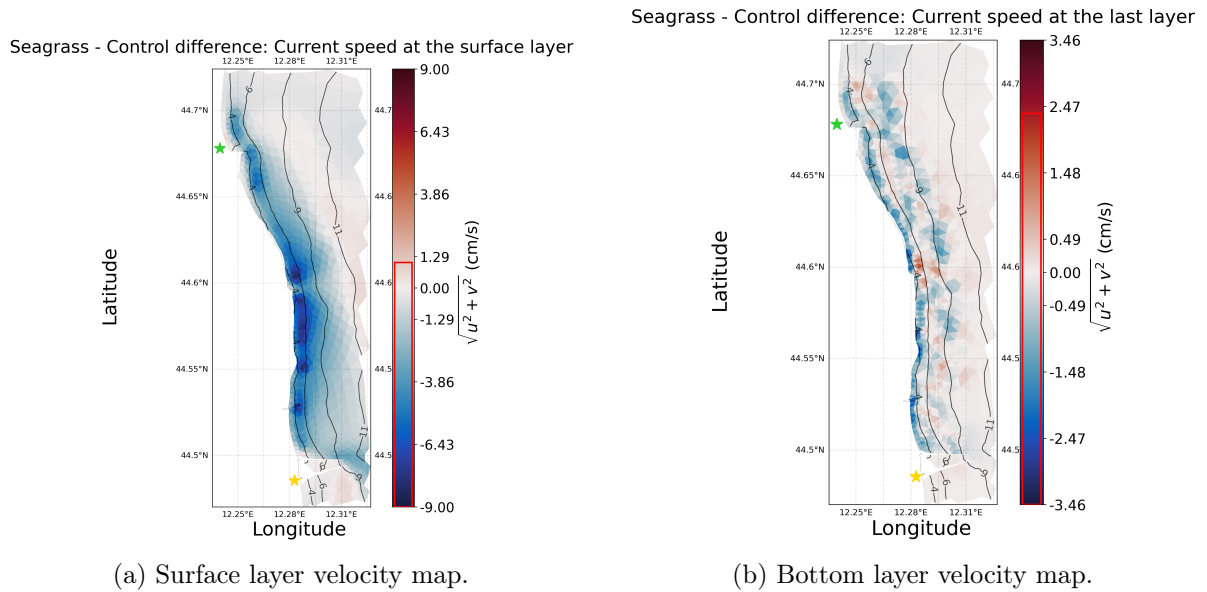
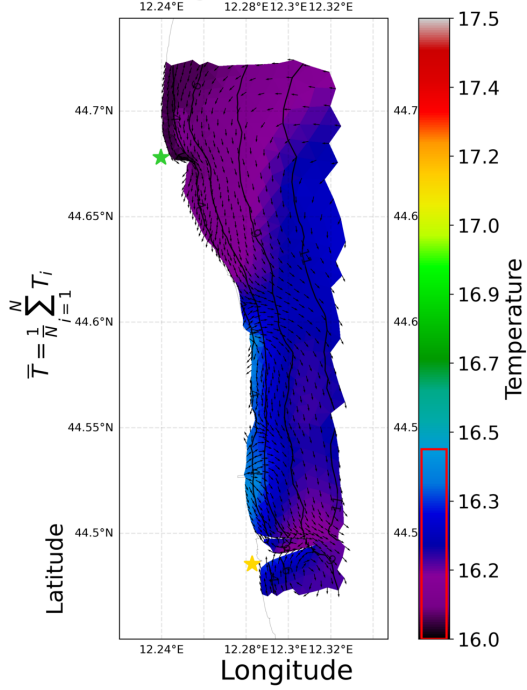


Figure 4.18: Time-averaged velocity magnitude maps for the difference (seagrass minus control).

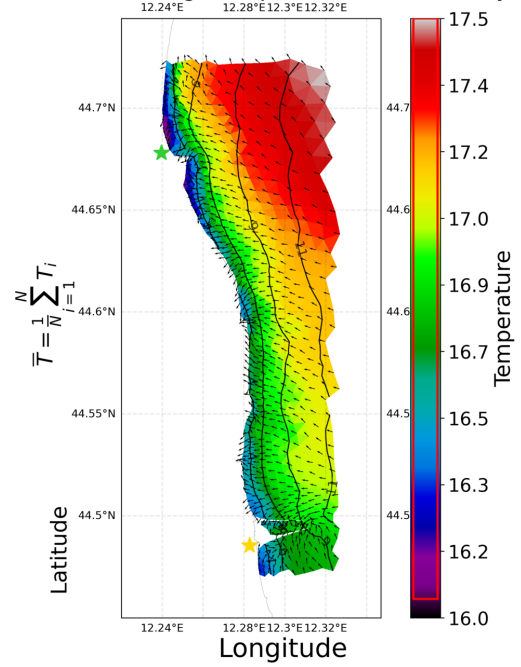
Temperature Figure 4.19 displays the time-averaged temperature maps for the "WiS-27" scenario, illustrating the difference between the seagrass and control conditions at both the surface and the last (bottom) layer. The surface temperature shows values ranging from 16 C to 16.5 C, exhibiting relatively uniform values across the region. In contrast, the bottom layer reveals more pronounced localized effects, with temperatures varying from 16 C to 17.5 C, peaking in the northern part of the map. The black arrows on both maps indicate current directions, which may contribute to the observed thermal patterns through advection.

WiS-27: Time average temperature at the surface



(a) Surface temperature map.

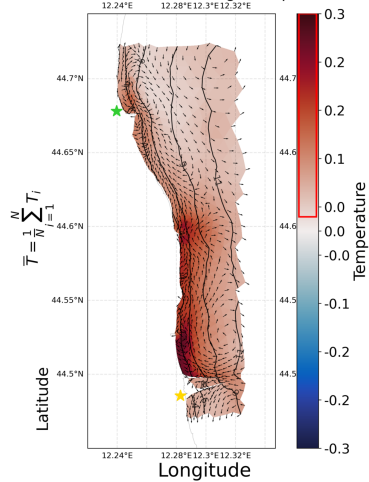
WiS-27: Time average temperature at the last layer



(b) Bottom temperature map.

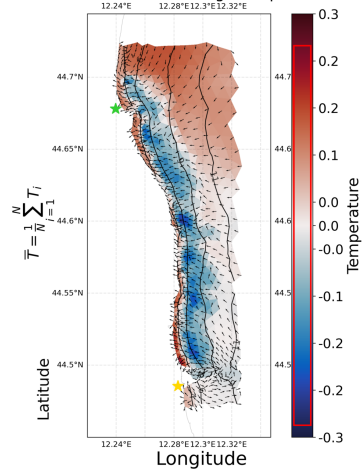
Figure 4.19: Time-averaged temperature maps for the seagrass model.

Seagrass - Control difference: Time average temperature at the surface



(a) Surface temperature map.

Seagrass - Control difference: Time average temperature at the last layer



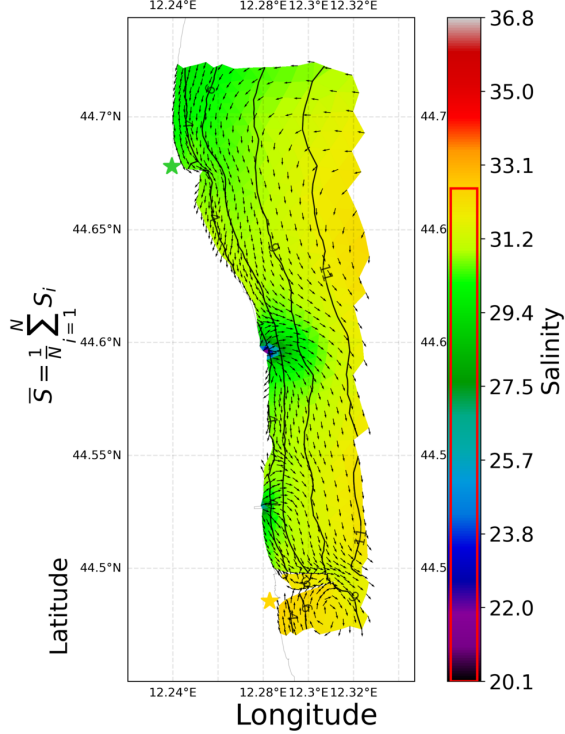
(b) Bottom temperature map.

Figure 4.20: Time-averaged temperature maps for the difference (seagrass minus control).

Figure 4.20 shows the time-averaged temperature maps for the difference between the "WiS-27" scenario and the Control models. It's evident that seagrass can enhance thermal stratification by modulating vertical mixing. Specifically, the seagrass canopy increases drag and reduces turbulence, which limits the upward and downward exchange of heat between the surface and deeper waters. As a result, the upper water layer tends to retain more of the solar energy absorbed at the surface, leading to a slight warming. The bottom layer, which is characterized by higher salinity and a stable density structure, experiences reduced heat transfer from the surface, allowing it to remain cooler. This differential effect contributes to a more pronounced temperature gradient within the water column, with warmer conditions at the surface and cooler conditions near the bottom in seagrass-dominated areas.

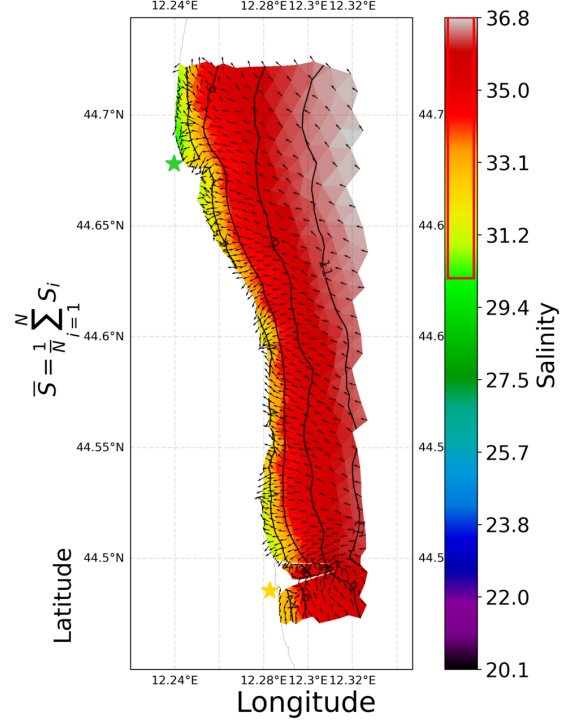
Salinity Figure 4.21 presents the time-averaged salinity maps for the "WiS-27" scenario. At the surface, salinity exhibits a small spatial variability, with values generally ranging from 29.4 psu to 32 psu, except for areas in proximity to riverine mouths. In contrast, the bottom layer reveals higher values, with salinity ranging from 30 to 37 psu, with the lowest values exclusively present near the coast. The black arrows on both maps indicate current directions, which contribute to the observed salinity patterns through advection and mixing dynamics.

WiS-27: Time average salinity at the surface



(a) Surface layer salinity map.

WiS-27: Time average salinity at the last layer

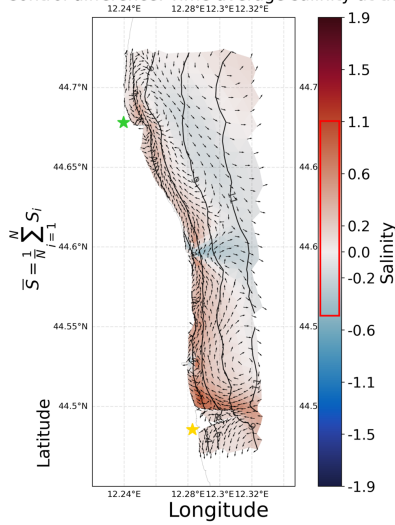


(b) Bottom layer salinity map.

Figure 4.21: Time-averaged salinity maps for the seagrass model.

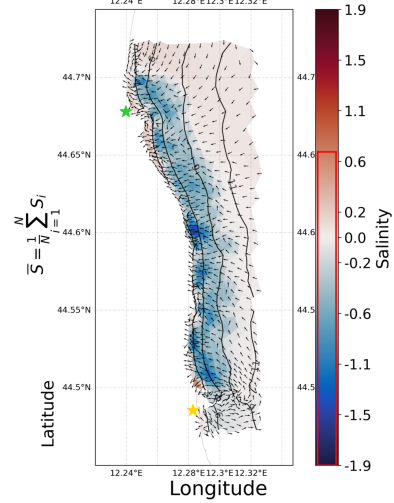
Figure 4.22 presents the time-averaged salinity maps for the difference between the seagrass scenario and the Control model. The seagrass-only analysis shows increased salinity at the surface layer near the coast, while a slight negative difference is evident where the Reno river enters the Adriatic. At the bottom layer, the differences highlight that seagrass tends to reduce mixing dynamics, locally increasing freshwater retention, hence reducing the yearly average value.

Seagrass - Control difference: Time average salinity at the surface



(a) Surface layer salinity map.

Seagrass - Control difference: Time average salinity at the last layer



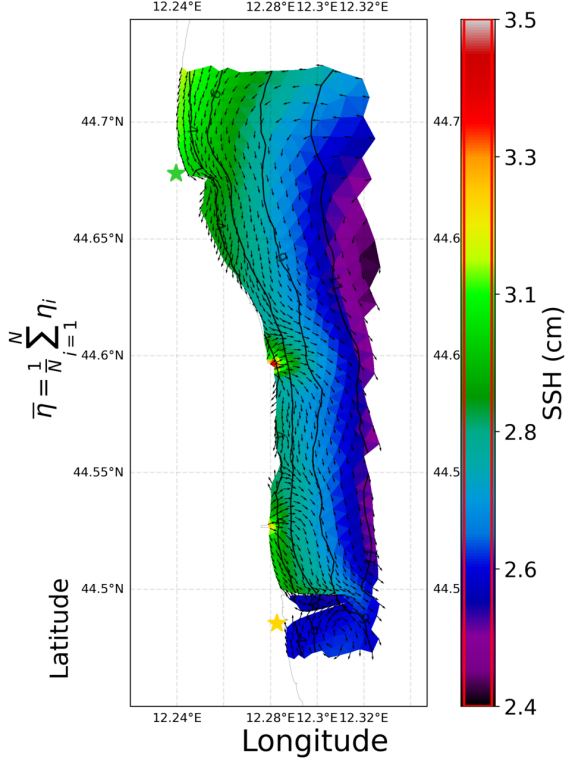
(b) Bottom layer salinity map.

Figure 4.22: Time-averaged salinity maps for the difference (seagrass minus control).

Sea Surface Height Map Figure 4.23a shows the time averaged sea surface height map for the "WiS-27" model. The effect of the Reno river on the sea surface height can be seen as a red spot near the center of the map. In the north and in the south of the region, the current direction lines suggest that a higher sea surface height may be explained by water accumulation against a solid barrier, respectively the Bellocchio beach, and the coast north of Marina di Ravenna harbor.

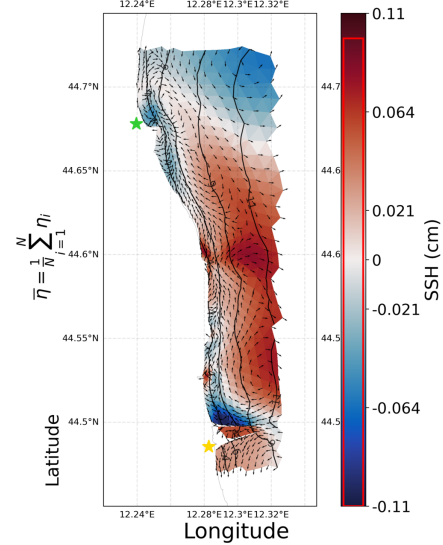
Figure 4.23b indicates the yearly average of sea surface height differences between the "WiS-27" and control scenarios. Positive differences occur primarily near riverine outputs, while negative differences are concentrated in the northern regions and next to the harbor walls of Marina di Ravenna. These patterns reflect the influence of seagrass on local hydrodynamics, including increased drag, altered currents (indicated by black arrows), and bathymetric effects, resulting in localized changes in sea surface height.

WiS-27: Time average sea surface height



(a) Sea surface height map of "WiS-27"

Seagrass - Control difference: Time average sea surface height



(b) Bottom layer salinity map.

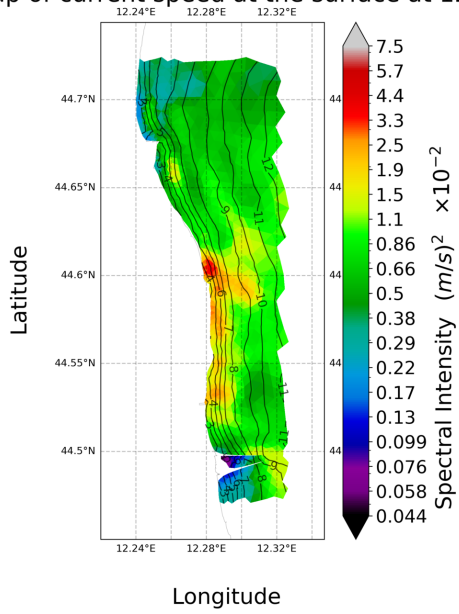
Figure 4.23: Time-averaged salinity maps for the difference (seagrass minus control).

Spectral Analysis

Figures 4.26 and 4.27 show the spectral transformation intensity maps of current velocity for the seagrass scenario at 12 h and 24 h periods, respectively. The maps indicate that seagrass tends to dampen high-frequency fluctuations (e.g., 12 h) due to increased bottom friction, while the tidal (24 h) signals remain largely dominant.

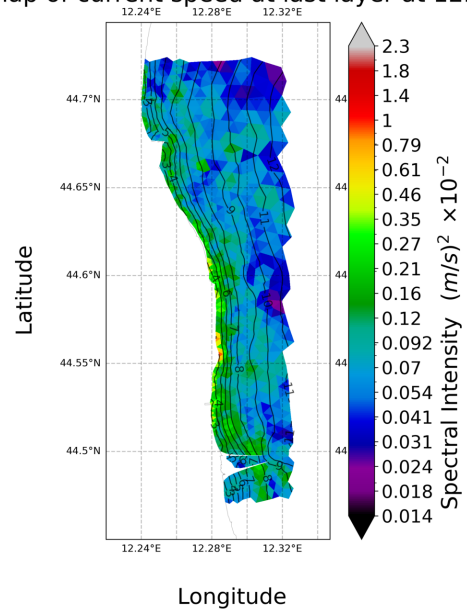
Figures 4.24 and 4.25 illustrate the spectral transformation intensity maps of current velocity, for the difference between the seagrass scenario and the control models at 12 and 24 hours periods. At a 12-hour period, the maps reveal that the high-frequency fluctuations are moderately damped in areas where seagrass is present, indicating that the seagrass effectively reduces the amplitude of rapid oscillations. In contrast, at the 24-hour period—associated primarily with tidal dynamics—the spectral intensity remains robust, suggesting that while seagrass moderates higher-frequency turbulence, it has a less pronounced effect on the dominant tidal signals. This differential modulation highlights the role of seagrass in selectively damping small-scale, high-frequency processes while allowing larger-scale tidal flows to persist.

Seagrass - Control difference spectral intensity map of current speed at the surface at 12h per



(a) Surface spectral map (12 h).

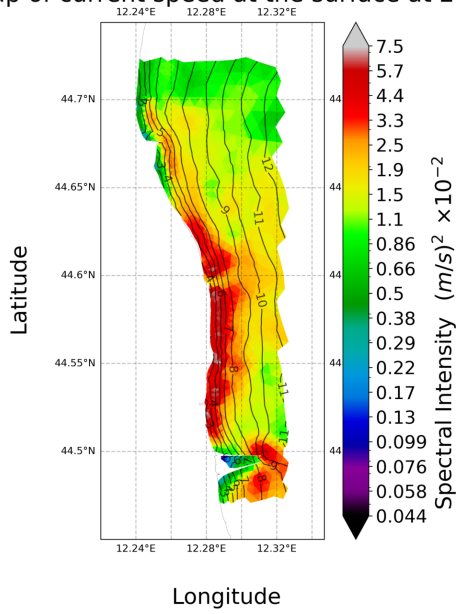
Seagrass - Control difference spectral intensity map of current speed at last layer at 12h per



(b) Bottom spectral map (12 h).

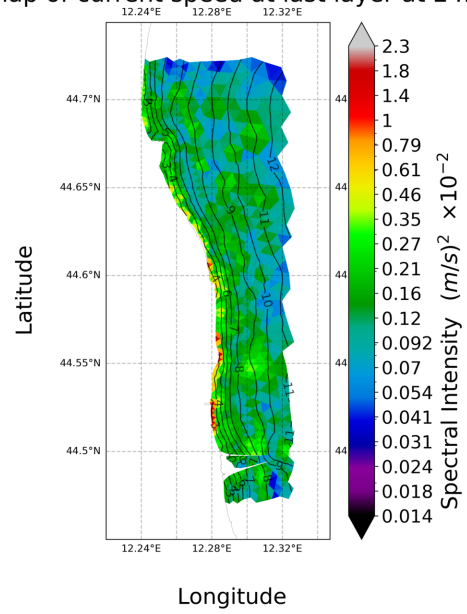
Figure 4.24: Spectral transformation intensity maps for the difference (seagrass minus control) at 12 h.

Seagrass - Control difference spectral intensity map of current speed at the surface at 24h period



(a) Surface spectral map (24 h).

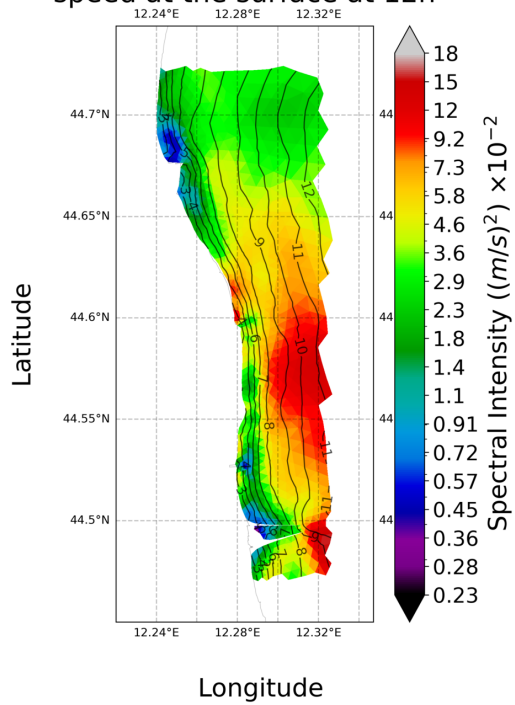
Seagrass - Control difference spectral intensity map of current speed at last layer at 24h period



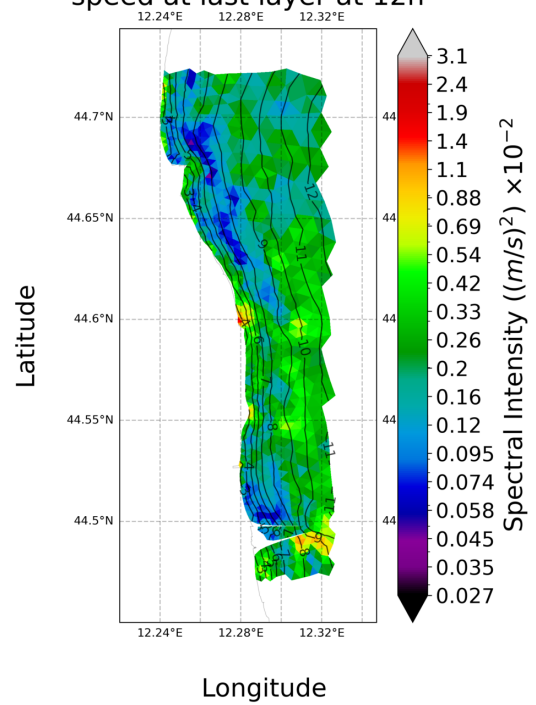
(b) Bottom spectral map (24 h).

Figure 4.25: Spectral transformation intensity maps for the difference (seagrass minus control) at 24 h.

WiS-27 spectral intensity map of current speed at the surface at 12h



WiS-27 spectral intensity map of current speed at last layer at 12h

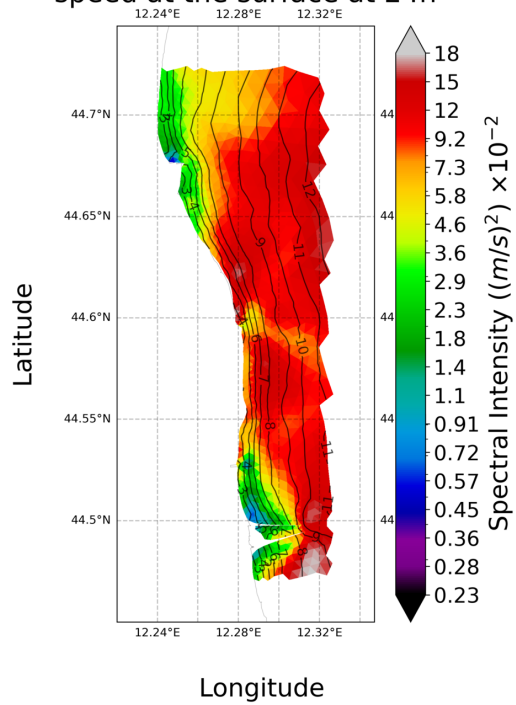


(a) Surface spectral map (12 h) at the surface.

(b) Bottom spectral map (12 h) at the bottom.

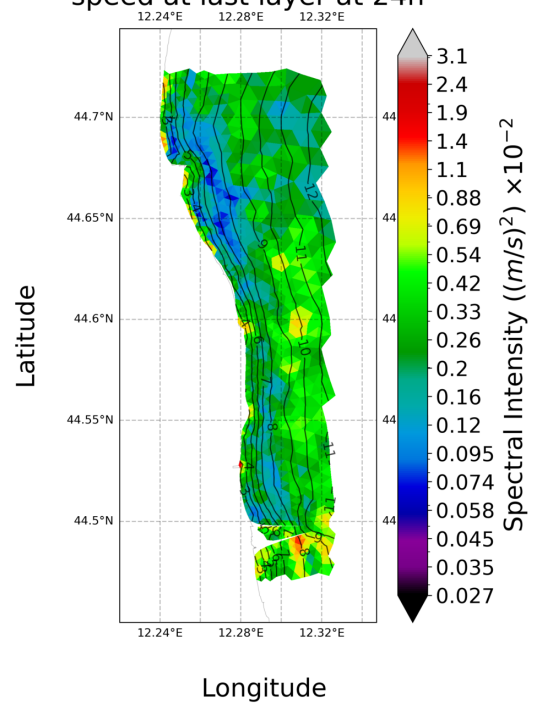
Figure 4.26: Spectral transformation intensity maps for the seagrass model.

WiS-27 spectral intensity map of current speed at the surface at 24h



(a) Surface spectral map (12 h).

WiS-27 spectral intensity map of current speed at last layer at 24h



(b) Bottom spectral map (24 h).

Figure 4.27: Spectral transformation intensity maps for the seagrass model.

Chapter 5

Ensemble of seagrass models

This analysis will be conducted considering the ensemble composed of seagrass models. The standard deviation of ensemble members is chosen as an effective way of observing the impact of seagrass on the hydrodynamics of the basin. The standard deviation of the ensemble is systematically computed and averaged among the different seagrass parametrization models. This analysis will highlight the sensitivity of each variable, for the different seagrass modelizations in the ensemble.

5.1 Basin-Averaged Temperature and Salinity

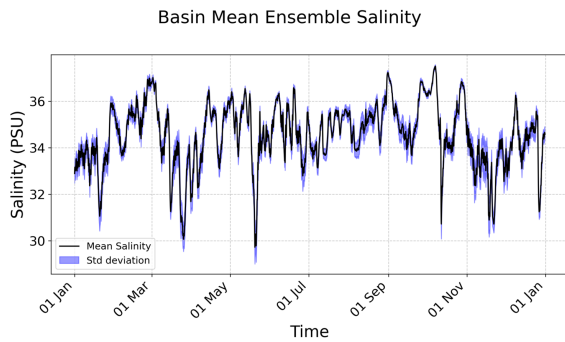
Figure 5.1 presents the ensemble standard deviation in basin-integrated salinity and temperature between the ensemble elements (models 1–27). The x-axis represents time, while the left and right y-axes show the ensemble mean salinity and temperature, respectively. Additionally, the blue lines represent the corresponding standard deviation around the mean.

The time series in Figure 5.1 indicates that the variability associated with the ensemble members' influence on basin-integrated salinity and temperature is generally small. This suggests that, on a basin-wide scale, each seagrass scenario chosen in our ensemble has mostly the same effect.

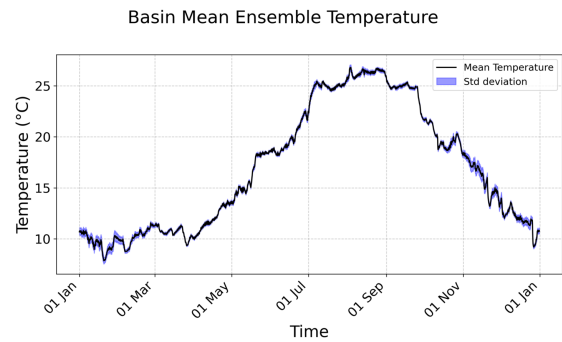
5.2 Hovmöller Diagrams of Differences

Here the time series of horizontally averaged vertical profiles of salinity and temperature for the standard deviation computed over the ensemble members is shown in its vertical and temporal dependence.

In figure 5.2 it appears that the most significant ensemble differences occur in the upper water column, where seagrass influences salinity and slightly alter the temperature gradient. In deeper layers, differences are more localized and generally comparable to



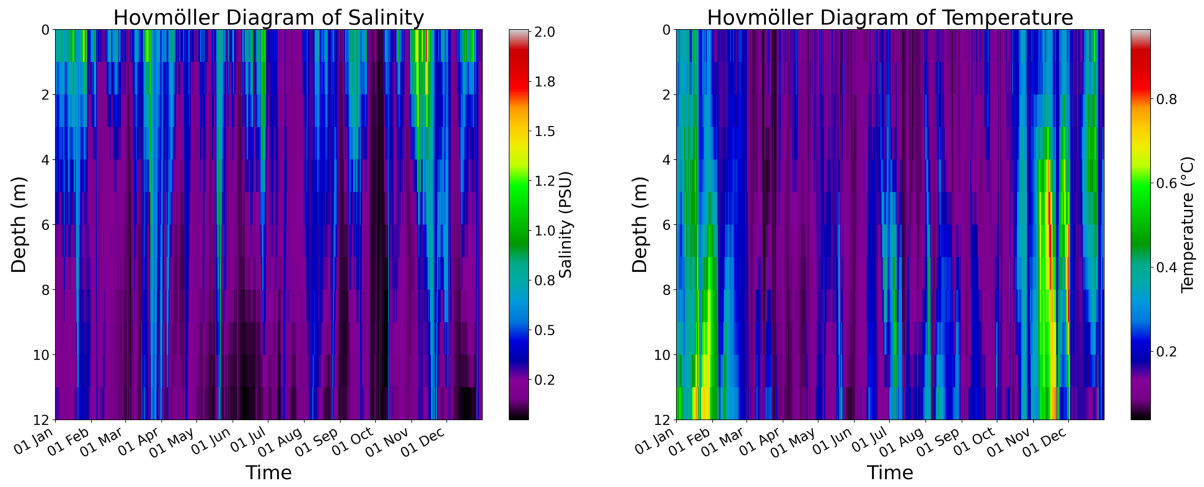
(a) Basin-integrated salinity and its standard deviation at the surface.



(b) Basin-integrated temperature and its standard deviation at the bottom

Figure 5.1: Ensemble standard deviation in basin-averaged salinity and temperature.

the difference between the "WiS-27" and control models, suggesting that the influence of seagrass for basin integrated properties is not altered by leaf length, leaf width and leaf surface density.



(a) Hovmöller diagram of standard deviation for salinity.

(b) Hovmöller diagram of standard deviation for temperature.

Figure 5.2: Hovmöller diagrams of the standard deviation of ensemble members for salinity and temperature averaged horizontally.

5.3 Horizontal maps of Ensemble STD at Surface and Bottom Layers

The following figures present the time average of sea surface height, velocity, temperature, and salinity at both the surface and bottom layers. Each figure is obtained using the standard deviation of the ensemble and characterizes the horizontal sensitivity of seagrass parametrization over the area of interest.

5.3.1 Velocity STD

In figure 5.3, the time-averaged standard deviation of current speed among ensemble members indicates a substantial variability in proximity of seagrass distribution and particularly near the coast, where the water column height is comparable to the leaves length. After observing that this variability is comparable to the seagrass minus control model difference, it can be concluded that our seagrass parameters have an influence on the average velocity reduction observed.

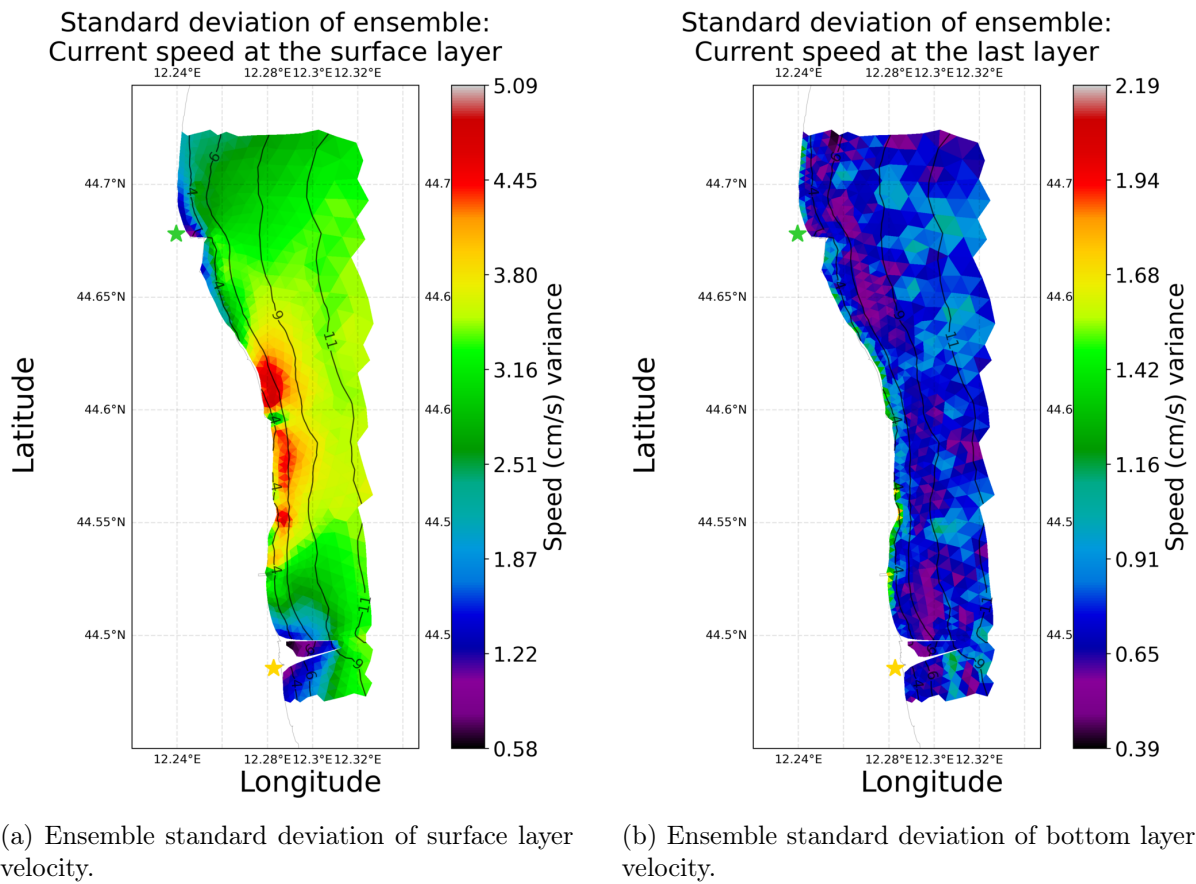
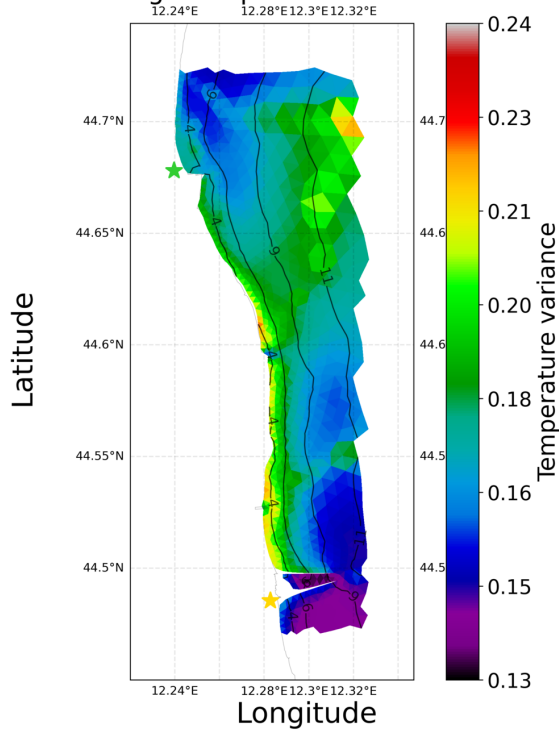


Figure 5.3: Time-averaged current velocity of the standard deviation of the ensemble.

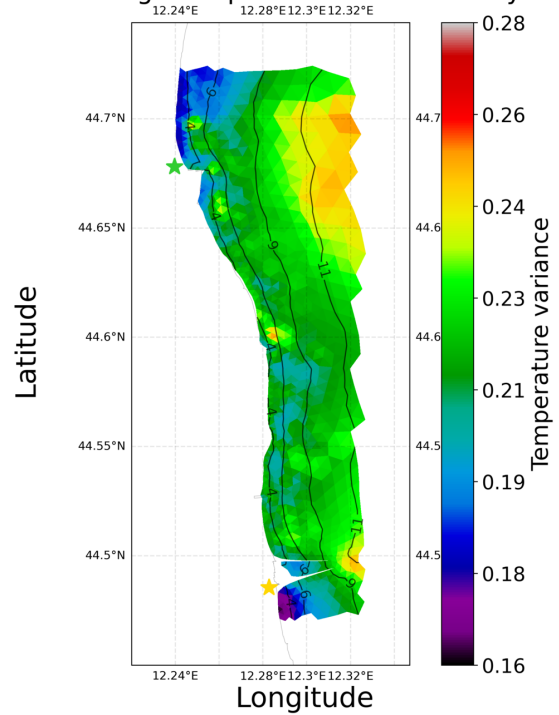
Temperature STD The ensemble standard deviation maps of the yearly average temperature (fig. 5.4) reveal substantial variability among ensemble members, indicating that seagrass influences the overall thermal structure at both the surface and bottom layers. In particular, at the bottom layer, regions with seagrass patches exhibit a markedly higher standard deviation. This pronounced variability is probably linked to longer water renewal times within these patches, suggesting slower water exchange, diminished heat transfer, and, as a result, localized lower temperatures.

Standard deviation of ensemble:
Time average temperature at the surface



(a) Surface layer temperature.

Standard deviation of ensemble:
Time average temperature at the last layer



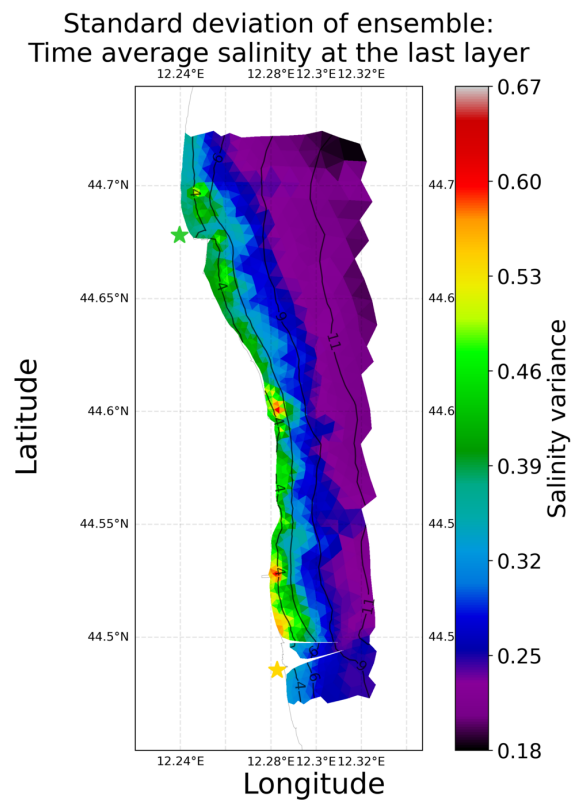
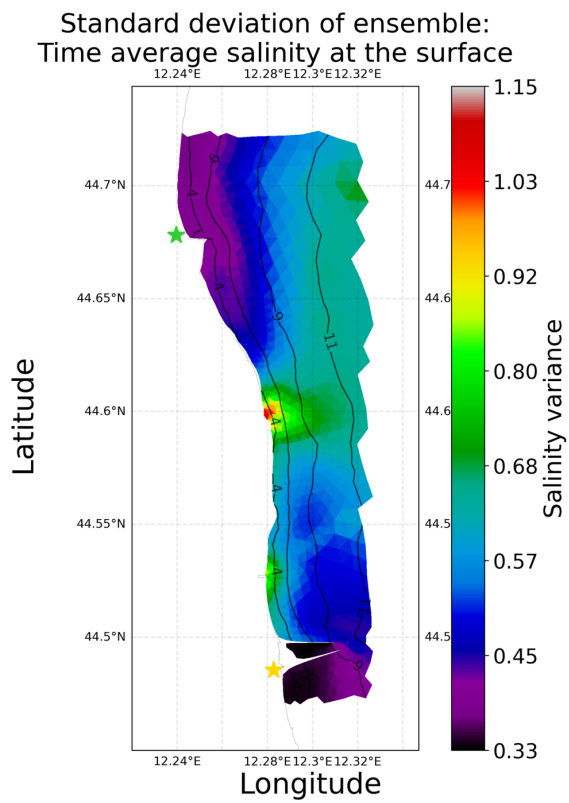
(b) Bottom layer temperature.

Figure 5.4: Time-averaged temperature of the standard deviation of the ensemble.

5.3.2 Salinity STD

The salinity maps in figures 5.5 suggest that differences among ensemble members are more pronounced near river mouths at the surface level. It can be observed that both the surface layer map and the bottom layer map, have standard deviations values which are comparable to the difference between "WiS-27" scenario and control models. This indicates that seagrass can affect salinity by altering local mixing and retention processes.

5.3.3 Sea Surface Height STD



(a) Surface layer salinity.

(b) Bottom layer salinity.

Figure 5.5: Time-averaged salinity of the standard deviation of the ensemble.

Standard deviation of ensemble:
Time average sea surface height

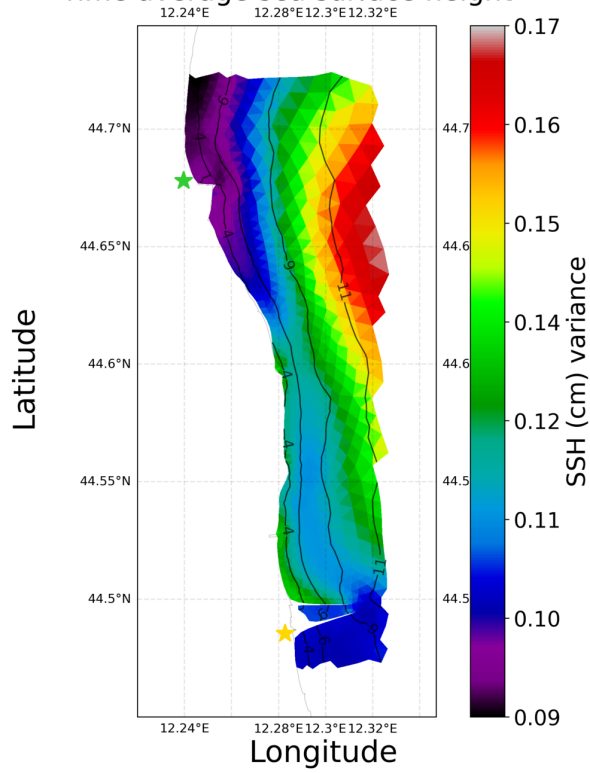
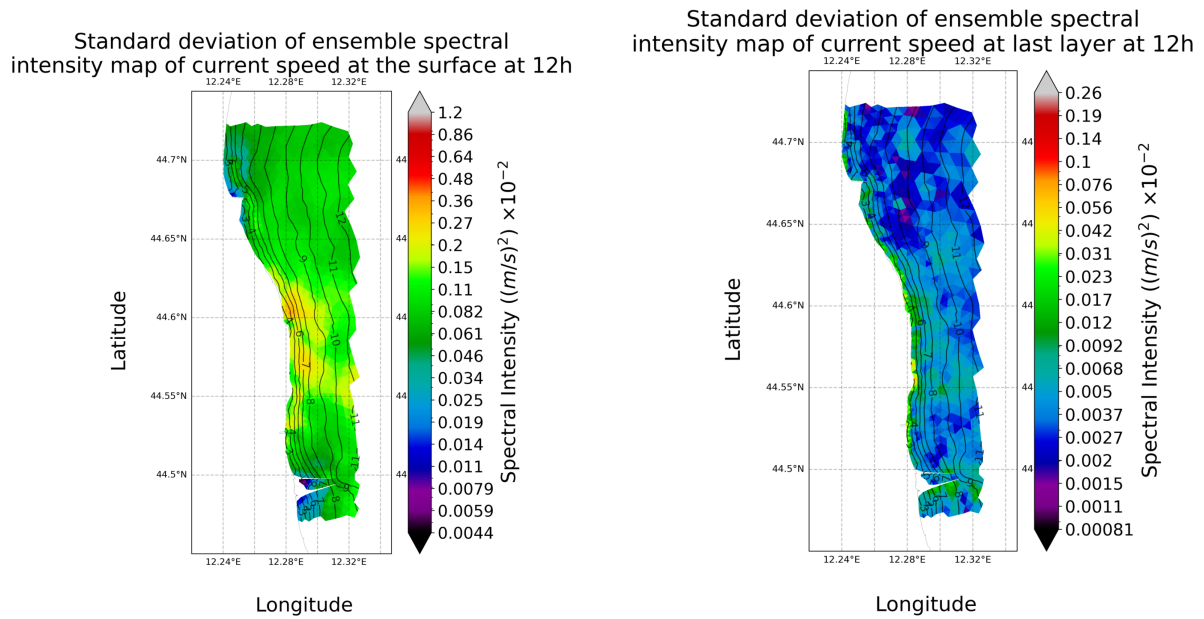


Figure 5.6: Sea surface height map (in *cm*).

As its shown in figure 5.6, the ensemble standard deviation of sea surface height is substantial, compared to the differences between the "WiS-27" and control models. The variability observed reflects the sea surface height sensitivity due to the seagrass parametrization chosen.

5.4 Spectral Analysis of Ensemble STD

Figures 5.7a and 5.8a present the spectral-transformation intensity maps of ensemble-standard-deviation in current speed at the surface for 12 h and 24 h, respectively, while Figures 5.7b and 5.8b show analogous maps at the bottom layer. The spectral analysis indicates that, at both 12 h and 24 h, the highest variability is concentrated along the coastline. In the surface maps, there is a distinct gap around the mouth of the Reno River, with the largest standard deviations aligned near the shore. At the bottom layer, the variability tends to be lower overall but exhibits multiple localized “hot spots” of higher standard deviation, suggesting that benthic features such as seagrass meadows exert a pronounced influence on current-speed fluctuations in those areas.

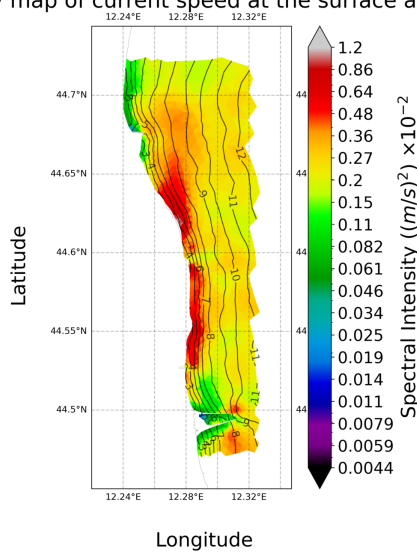


(a) Current velocity spectral intensity at 12 h at the surface layer.

(b) Current velocity spectral intensity at 12 h at the bottom layer.

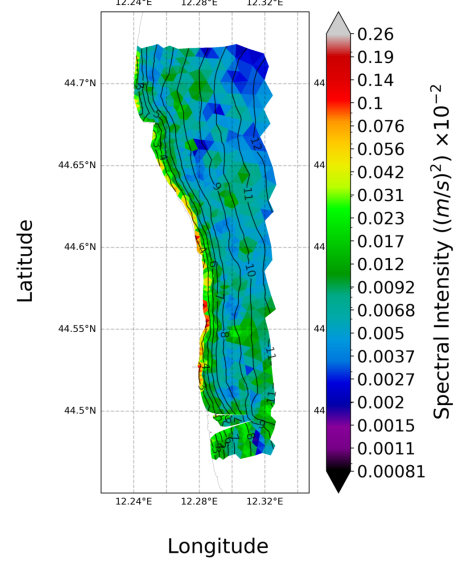
Figure 5.7: Spectral transformation intensity maps of the ensemble standard deviation in current velocity at 12 h period at the surface (left) and bottom layers (right).

Standard deviation of ensemble spectral intensity map of current speed at the surface at 24h



(a) Current velocity spectral intensity at 24 h at the surface layer.

Standard deviation of ensemble spectral intensity map of current speed at last layer at 24h



(b) Current velocity spectral intensity at 24 h at the bottom layer.

Figure 5.8: Spectral transformation intensity maps of the ensemble standard deviation in current velocity at 24 h period at the surface (left) and bottom layers (right).

Chapter 6

Conclusions

This research indicates that seagrass plays a significant role in modulating the salinity distribution across the water column through a combination of physical and hydrological processes. Locally, the presence of seagrass leads to a decrease in salinity at the bottom due to freshwater retention; the seagrass canopy acts to trap incoming freshwater, limiting its mixing with the saltier deep water. In contrast, at the surface, reduced vertical mixing—combined with increased sun exposure, which enhances evaporation—results in a higher salinity level. These processes collectively cause a decrease in potential density in the affected areas, as lower salinity corresponds to lower water density, particularly near the surface. This outcome underscores the complex interplay between seagrass-induced physical barriers and the hydrodynamic processes that govern freshwater and saltwater distribution, ultimately influencing the stratification and ecological dynamics of the coastal environment.

The presence of seagrass leads to a noticeable reduction in current velocity, particularly near the bottom layers. This effect is primarily due to the increased drag exerted by the flexible seagrass blades, which act to dissipate energy from the flow. The flexible nature of the seagrass allows the blades to bend in response to water movement, thereby increasing friction and altering the momentum transfer in the near-bed region. Consequently, seagrass-dominated areas exhibit lower current speeds compared to not vegetated zones. This dynamic behavior underscores the significant role that seagrass plays in modulating local hydrodynamics.

The horizontal distribution of temperature and salinity reveals modest but discernible differences when seagrass is present. Horizontal maps of these variables show that seagrass tends to alter lateral mixing patterns, leading to localized shifts in water mass properties. These lateral differences are slightly more extended than those observed for current speeds, suggesting that seagrass influences the pathways of freshwater and saline water exchange along the coast. This effect likely stems from the increased friction and drag imposed by the seagrass canopy, which subtly redirects flow and modifies the local advection processes. As a result, the distribution of salinity and temperature exhibits

spatial variability that is more noticeable across the study region.

Additionally, subtle modifications in sea surface height (SSH) are observed in seagrass-dominated areas. Although the ensemble standard deviation of SSH is low overall, the slightly higher variability near the coast can be attributed to the altered coastal circulation dynamics induced by seagrass. These modifications in SSH reflect the combined effects of reduced nearshore mixing, modified advection patterns, and interactions with freshwater inputs. Even though these differences are small, they may have important implications for sediment transport and nutrient distribution in shallow coastal environments.

While this work highlights the contributions of seagrass to coastal hydrodynamics, several avenues for future implementation remain that could further enhance the model's ecological fidelity. For instance, incorporating sediment transport processes would allow us to more accurately predict how seagrass-mediated flow reductions contribute to sediment deposition and stabilization, thereby mitigating erosion. Additionally, integrating shading effects into the model could improve our understanding of light attenuation within seagrass canopies, which is critical for simulating primary production and the overall energy balance of the system. Finally, a more detailed representation of the nutrient cycle—capturing how seagrass uptake, recycling, and sediment interactions influence nutrient dynamics—would provide deeper insights into the ecosystem services offered by these habitats.

Chapter 7

Bibliography

Blumberg, A.F. and Mellor, G.L. (1987) A Description of a Three-Dimensional Coastal Ocean Circulation Model. In: Heaps, N.S., Ed., Coastal and Estuarine Sciences, Book 4, American Geophysical Union, 1-6.

Borum, J., Duarte, C.M., Krause-Jensen, D. and Greve, T.M. (eds.) (2004) European seagrasses: an introduction to monitoring and management. Monitoring and Managing of European Seagrasses Project (M&MS), 88pp. <https://doi.org/10.25607/0BP-1997>

Ondiviela, B., Fernández, L., Puente, A., García-Castrillo, G. and Juanes, J.A. (2018). Characterization of a resilient seagrass meadow during a decline period. *Scientia Marina*, 82(1), 67–75. <https://doi.org/10.3989/scimar.04616.18A>

Burchard, Hans & Bolding, Karsten & Ruiz-Villarreal, Manuel. (1999). GOTM, a general ocean turbulence model. Theory, implementation and test cases.

Clementi, E., Aydogdu, A., Goglio, A. C., Pistoia, J., Escudier, R., Drudi, M., Grandi, A., Mariani, A., Lyubartsev, V., Lecci, R., Cretí, S., Coppini, G., Masina, S., & Pinardi, N. (2021). Mediterranean Sea Physical Analysis and Forecast (CMEMS MED-Currents, EAS6 system) (Version 1) [Data set]. Copernicus Monitoring Environment Marine Service (CMEMS). https://doi.org/10.25423/CMCC/MEDSEA_ANALYSISFORECAST_PHY_006_

Danovaro, R., Fanelli, E., Aguzzi, J. et al. (2020). Ecological variables for developing a global deep-ocean monitoring and conservation strategy. *Nat Ecol Evol*, 4, 181–192. <https://doi.org/10.1038/s41559-019-1091-z>

Duarte, C. M., Marbà, N., Gacia, E., Fourqurean, J. W., Beggins, J., Barrón, C., & Apostolaki, E. T. (2010). Seagrass community metabolism: Assessing the carbon sink capacity of seagrass meadows. *Global Biogeochem. Cycles*, 24, GB4032. <https://doi.org/10.1029/2010GB003793>

Duarte, C., Losada, I., Hendriks, I. et al. (2013). The role of coastal plant communities for climate change mitigation and adaptation. *Nature Clim Change*, 3, 961–968. <https://doi.org/10.1038/nclimate1970>

Fofonoff, N.P. and Millard Jr, R.C. (1983). Algorithms for the computation of fundamental properties of seawater. Paris, France, UNESCO, 53pp. (UNESCO Technical Papers in Marine Sciences; 44). <https://doi.org/10.25607/OBP-1450>

Guidetti, Paolo & Buia, Maria & Lorenti, Maurizio & Scipione, Maria & Zupo, Valerio & Mazzella, Lucia. (2001). Seasonal Trends in the Adriatic Seagrass Communities of *Posidonia oceanica* (L.) Delile, *Cymodocea nodosa* (Ucria) Ascherson, *Zostera marina* L.: Plant Phenology, Biomass Partitioning, Elemental Composition and Faunal Features. https://doi.org/10.1007/978-88-470-2105-1_37

Hemminga, M.A. and Duarte, C.M. (2000). *Seagrass Ecology*. Cambridge University Press, Cambridge. <https://doi.org/10.1017/CB09780511525551>

Luhar, Mitul & Nepf, Heidi M. (2011). Flow-induced reconfiguration of buoyant and flexible aquatic vegetation. *Limnology and Oceanography*, 56. <https://doi.org/10.4319/lo.2011.56.6.2003>

Macic, V. (2014). Anatomical features of seagrass *Posidonia oceanica* (L.) Del. growing in Montenegro (Adriatic Sea). *Poljoprivreda i Sumarstvo*, 60(3), 55–64. <https://www.proquest.com/docview/1614349880>

Mazzella, Lucia & Guidetti, Paolo & Lorenti, Maurizio & Buia, Maria & Zupo, Valerio & Scipione, Maria & Rismondo, Andrea & Curiel, Daniele. (1998). Biomass partitioning in Adriatic seagrass ecosystems (*Posidonia oceanica*, *Cymodocea nodosa*, *Zostera marina*). *Rapp. Comm. int. Mer Médit.*, 35, 562–563.

McLeod, E., Chmura, G.L., Bouillon, S., Salm, R., Björk, M., Duarte, C.M., Lovelock, C.E., Schlesinger, W.H. and Silliman, B.R. (2011). A blueprint for blue carbon: toward an improved understanding of the role of vegetated coastal habitats in sequestering CO₂. *Frontiers in Ecology and the Environment*, 9, 552–560. <https://doi.org/10.1890/110004>

Orlić, M., Kuzmić, M., & Pasarić, Z. (1994). Response of the Adriatic Sea to the bora and sirocco forcing. *Continental Shelf Research*, 14(1), 91–116. [https://doi.org/10.1016/0278-4343\(94\)90007-8](https://doi.org/10.1016/0278-4343(94)90007-8)

Paulson, C. A., & Simpson, J. J. (1977). Irradiance Measurements in the Upper Ocean. *J. Phys. Oceanogr.*, 7, 952–956. [https://doi.org/10.1175/1520-0485\(1977\)007<0952:IMITU0>2.0.CO;2](https://doi.org/10.1175/1520-0485(1977)007<0952:IMITU0>2.0.CO;2)

Rabalais, N. N., Turner, R., Diaz, R. J., Justic, D. (2009). Global Change And Eutrophication Of Coastal Waters. *ICES Journal Of Marine Science*, 66(7), 1528–1537. <https://doi.org/10.1093/icesjms/fsp047>

Short, F., Carruthers, T., Dennison, W., & Waycott, M. (2007). Global seagrass distribution and diversity: A bioregional model. *Journal of Experimental Marine Biology and Ecology*, 350(1-2), 3–20. <https://doi.org/10.1016/j.jembe.2007.06.012>

Simberloff, D., Martin, J.-L., Genovesi, P. et al. (2013). Impacts of biological invasions: what's what and the way forward. *Trends in Ecology & Evolution*, 28(1), 58–66. <https://doi.org/10.1016/j.tree.2012.07.013>

Smagorinsky, J. (1963). General circulation experiments with the primitive equations. *Mon. Wea. Rev.*, 91, 99–164. [https://doi.org/10.1175/1520-0493\(1963\)091<0099:GCEWTP>2.3.CO;2](https://doi.org/10.1175/1520-0493(1963)091<0099:GCEWTP>2.3.CO;2)

Tagliapietra, Davide, Zanon, Veronica, Frangipane, Gretel, Umgiesser, Georg, & Sigovini, Marco. (2009). Zonazione fisiografica della Laguna di Venezia - Physiographic Zoning of the Venetian Lagoon.

IUCN (2020). Global Standard for Nature-based Solutions. A user-friendly framework for the verification, design and scaling up of NbS. First edition. Gland, Switzerland: IUCN.

Umgiesser, Georg, Canu, Donata, Cucco, Andrea, & Solidoro, Cosimo. (2004). A finite element model for the Venice Lagoon. Development, set up, calibration and validation. *Journal of Marine Systems*, 51, 123–145. <https://doi.org/10.1016/j.jmarsys.2004.05.009>

Vianello, A., Boldrin, A., Guerriero, P., Moschino, V., Rella, R., Sturaro, A., & Da Ros, L. (2013). Microplastic particles in sediments of Lagoon of Venice, Italy: First observations on occurrence, spatial patterns and identification. *Estuarine, Coastal and Shelf Science*, 130, 54–61. <https://doi.org/10.1016/j.ecss.2013.03.022>